NTNU

Norwegian University of
Science and Technology

Extracellular matrix modifications by oligoguluronates for cancer treatment

Bente Haug

Biotechnology (5 year)
Submission date: May 2018
Supervisor: Kurt Ingar Draget, IBT
Co-supervisor: Catherine T Nordgård, IBT

Norwegian University of Science and Technology
Department of Biotechnology and Food Science

Preface

This master thesis was conducted at the Institute of Biotechnology and Food Science at the Norwegian University of Science and Technology (NTNU) in the time-period September 2017 to May 2018.

I would like to thank my supervisors Dr. Catherine T. Nordgård and Professor Kurt I. Draget for introducing me to a very interesting topic of research. With their thoughtful help and encouragement throughout the project they have guided me through the ups- and downs of academic work. A grate thanks goes to Senior Engineers Astrid Bjørkøy and Ann-Sissel Teialeret Ulset for their technical assistance on confocal microscopy and spectrophotometry, and to Olav Andreas Aarstad for running the HPEAC-PAD analysis.

Lastly I would like to thank my fellow students, friends and family for the moral support, and their great help with and interest in my project.

Trondheim, May 15th 2018

Bente Haug

Abstract

Type I collagen is the main structural protein of the extracellular matrix, and is abnormally produced in many types of solid tumours. The presence of a thick and linearised collagen fibres constituting a dense network in a tumours micro-environment has been linked to high malignancy and chemoresistance of cancers. Rixova is a novel drug-candidate based on G-blocks that has demonstrated promising results in normalising the extracellular matrix, reducing tumour growth and enhancing drug delivery in preliminary clinical studies. This thesis investigates the modifications of collagen network structure and viscoelastic properties by treatment with G-blocks, which are highly defined and short, bioactive guluronate oligomers derived from alginate.

The effect of G-blocks on the fibrillation of type I tropocollagen monomers was investigated by simultaneous timelapse confocal reflectance microscopy visualising the structure of the collagen network, and by multiple-particle tracking with mean-square displacement- analysis measuring the microrheology of the solution. This new method of monitoring the sol-gel transition combines two established techniques and has provided accurate information about the relation between structure and viscoelasticity of the collagen network during gelation. This tool can potentially be used to study the sol-gel transition of other biopolymer-systems.

The study determined that short chained G-blocks with a DPn=12 had the strongest effect on collagen, accelerating the formation of initial aggregates in fibrillogenesis. The premature aggregation resulted in a final-network structure where fibers with larger diameters were organised in a more intertwined and densely connected network. Corresponding to the accelerated development of fibres, there was an accelerated development of viscoelastic properties of the gel. With increasing G-block concentrations the suspended particles exhibited earlier sub-diffusive motion patterns due to increasing viscosity of the fluid within pores of the network and increasing confinement by the surrounding network-structures.

In this thesis, G-blocks have been observed to interact with type 1 tropocollagen monomers, modulating the network-structure forming a stiffer and less penetrable matrix. This does not fully explain the beneficial effects seen in clinical studies of Rixova, so the mechanism behind the effect of G-blocks *in vivo* is yet to be determined. Further studies need to be performed to narrow down the knowledge gap between the results observed on *in vivo* and *in vitro* systems.

Sammendrag

Type I kollagen er det viktigste strukturelle proteinet i den ekstracellulære matriksen, og har utvist abnormal produksjon i fler typer kreftsvulster. Tilstedeværelsen av tykke og lineære kollagenfibre som utgjør et tett nettverk i tomor mikromiljøet har vært knyttet til økt ondartethet og kjemoresistens i kreft. Rixova er en ny legemiddelkandidat basert på G-blokker som har utvist lovende resultater ved å normalisere den ekstracellulære matrisen, redusere tumorvekst og øke legemiddelseffektivitet i kliniske studier. Denne oppgaven undersøker modifikasjoner av kollagenets nettverksstruktur og viskoelastiske egenskaper ved behandling med G-blokker, svært definerte og korte, bioaktive guluronatoligomerer fra alginat.

Effekten av G-blokker på fibrillering av type I-tropokollagenmonomerer ble undersøkt ved samtidig timelapse- konfokalreflektansmikroskopi som synliggjør strukturen av kollagennettverket, og multiple particle tracking med mean-square displacement -analyse som måler mikrorheologien i prøven. Denne nye metoden for overvåkning av sol-gel-overgangen kombinerer to etablerte teknikker, og har gitt nøyaktig informasjon om sammenhengen mellom struktur og viskoelastisitet av kollagennettverket i geleringsforløpet. Dette verktøyet kan potensielt brukes til å studere sol-gel-overgangen til andre biopolymer-systemer.

Studien har fastslått at kortkjedede G-blokker med DPn = 12 hadde den sterkeste effekten på kollagen, ved å akselerere dannelsen av de første aggregatene i fibrillogenese. Den premature aggregering resulterte i en endelig nettverksstruktur der fibrene med større diametre ble organisert i et mer sammenflettet og tett- koblet nettverk. I samsvar med den akselererte utviklingen av fibre, var det en akselerert utvikling av viskoelastiske egenskaper av gelen. Med økende konsentrasjoner av G-blokk utviste de suspenderte partiklene tidligere et sub-diffusjonellt bevegelsesmønster på grunn av økende viskositet av væsken i nettverksporene og økende restriksjon fra de omkringliggende nettverksstrukturene.

I denne oppgaven har det blitt observert at G-blokker interagerer med type 1 tropokollagenmonomerer, hvilket endrer nettverksstrukturen og gir en stivere og mindre gjennomtrengelig matrise. Dette kan dermed ikke fullt ut forklarer de gunstige effektene observert i kliniske studier av Rixova, så mekanismen bak effekten av G-blokkene textit in vivo er ennå ikke bestemt. For å oppnå en bedre forståelse av forskjellene mellom G-blokks påvirkning på textit in vivo og textit in vitro systemer trengs ytterlige studier.

Abbreviations

$< \alpha >$-value   Ensemble average anomalous exponent

$< MSD >$ Ensemble average Mean Square Displacement

α-value   Anomalous exponent

τ Timescale, or lag-time between frames

D_{eff} Effective diffusivity

F_G Fraction of guluronate monomers

F_M Fraction of mannuronate monomers

CAF   Cancer associated fibroblasts

CRM   Confocal Reflectance Microscopy

DPBS   Dulbecco's Phosphate Buffer Saline

DPn   Number average degree of polymerisation

DPw   Weight average degree of polymerisation

ECM   Extracellular matrix

EMT   Epithelial mesenchymal transition

G-block   Homoguluronate alginate

GAG   Glycosaminoglycan

HPAEC-PAD	High performance anion exchange chromatography with pulsed amperometric detection
LOX	Lysysyl oxidase
M-block	Homomannuronate alginate
MG-block	Alternating maunuronate and guluronate alginate
MMP	Matrix metalloprotein
MPT	Multiple Particle Tracking
MSD	Mean Square Displacement
Mw	Molecular weight
NMR	Nuclear Magnetic Resonance
PG	Proteoglycan
TL-CRM	Time-lapse Confocal Reflectance microscopy
TME	Tumour Microenvironment

Contents

1 Scientific Introduction

Cancer is the second leading cause of death worldwide causing an estimated 8.2 million deaths in 2012 [1]. It is a genetic disease, caused by malignant mutations leading to uncontrolled cell growth. Today, it has become widely accepted that not just the cancer cells, but also the tumour microenvironment (TME) plays an important part in the progression of solid tumours [2–4]. In addition to the cancer cells, a tumour also consists of recruited and corrupted "normal" cells such as immune cells, fibroblasts, pericytes, endothelial cells, adipocytes, and mesenchymal stem cells. In addition the interstitial fluids and extracellular matrix (ECM) surrounding these cells play an essential part [4]. The TME has a complex and active role in tumour-development, affecting the growth, proliferation, invasion and metastasis of cancer. In this thesis the effect of a potential antitumour agent affecting collagen, the major constituent of the ECM will be explored.

1.1 The Extracellular Matrix

The ECM is a complex network of macromolecules that are produced locally by the embedded cells and secreted into the interstitial space [5]. These extracellular molecules fill the space between cells, and provide them with structural and biochemical support. The ECM of different tissues may differ in organization and amount of types of constituents to serve the specific needs of that tissue type, yet they all have the same general composition [5]. There are three major classes of macromolecules that make up the ECM; the glycosaminoglycans (GAGs), the glycoproteins and the fibrous proteins as illustrated in figure 1.

The GAGs are carbohydrate polymers, usually covalently attached to the cell-membrane proteins to form proteoglycans, (with the exception of hyaluronan which forms non-covalently linked complexes with proteoglycans). The polysaccharide chains of GAGs are composed of a repeating disaccharide unit of an amino-sugar and a uronic acid. A notable exception is keratan which contains galactose instead of a hexuronic acid. The carboxyl-groups of the uronic acids, and sulfations gives the polymer a negative charge, resulting in an extended conformation because of electrostatic repulsion. The charge attracts co-ions, making the polymer-solution osmotically active, thus attracting water and forming a hydrogel. This gel can resist some compressive forces because of the turgor pressure of the gel. Within this proteoglycan-gel "ground substance", the glycoproteins and fibrous proteins
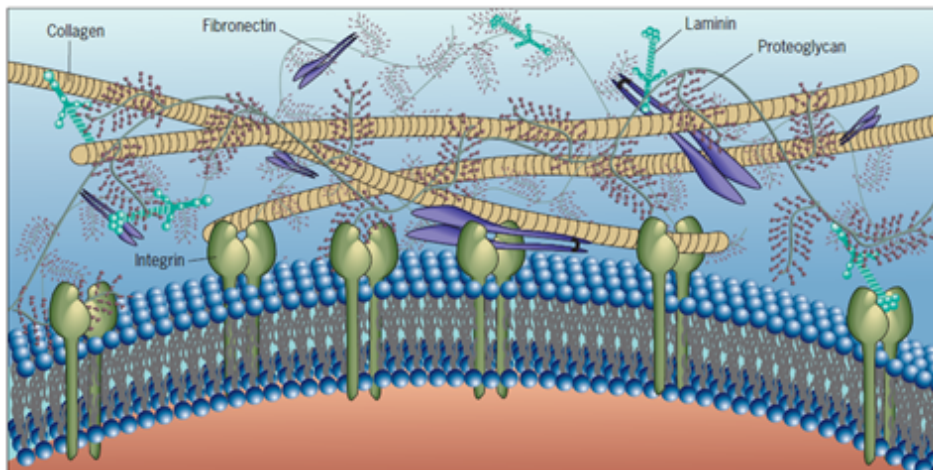
Figure 1: The main components of the ECM. The proteoglycans form a hydrogel in which the glycoproteins (fibronectin and laminin), and the fibrous proteins(collagen) are embedded. From: [6]

are embedded, forming a network which provides the strength and elasticity of the ECM [5].

The glycoproteins laminin and fibronectin, serve as adhesion proteins, mediating the connection between GAGs, fibrous proteins, to other glycoproteins and to the integrins of the cell membrane (see figure 1). The fibrous proteins provide the tensile strength to the tissue, and mediate the interaction between the ECM and the cell. As an example the fibrous protein elastin will, as the name implies, provide elasticity to the tissue by forming a flexible network of fibre-strands. Fibrillar collagens are the major structural component of the ECM, providing tensile strength to the tissue by forming an interconnected fibre-network [5].

1.1.1 Collagen

Collagens are the major constituents of the ECM. They are the most abundant protein in mammals, and can represent up to 30% of total protein mass [5]. Their main function is providing mechanical stability, which is why they are present in ample amounts in tissues requiring strength and flexibility such as tendon, skin and bone [7]. More than 40 genes for the expression of collagen have been described in human and mouse genome, combining to form 28 unique types of collagen [8]. The

most common are the fibrillar collagens, type I, II, III, V, XI, that can assemble into strong fibres providing three-dimensional framework for tissues and organs. The non-fibrillar collagens serve other functions in the ECM, such as type IV which is a constituent of the basal lamina, and the fibril associated collagens type VI and IX mediating cell-ECM interactions [5].

Type 1 collagen is the main structural protein of the ECM, making up 90% of the fibrous proteins. It is produced primarily by fibroblasts but also by other cells in the matrix, and secreted into the intracellular space where it self-assembles into a complex fibrillar network [8]. The polypeptide consists of repeats of the triple amino-acid sequence [Glycine–X–Y], where X and Y often are the imino-acids proline and hydroxyproline, respectively [7]. This composition of relatively small amino-acids enables the formation of a tightly coiled left-handed helix as depicted in figure 2, called an α-chain [5]. The twisted chain of 1050 aminoacid-residues has approximately 3.3 residues per turn, and a unit twist of about 180° [7].
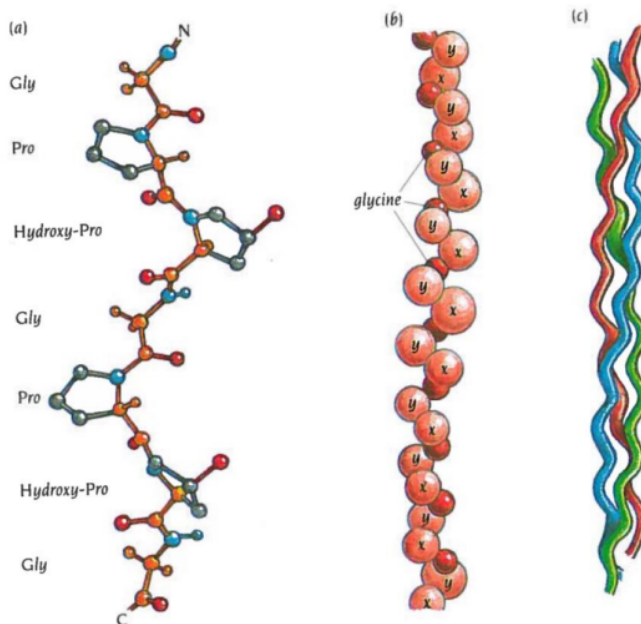

Figure 2: The left handed helical α-chains can associate into a procollagen triple-helix. The procollagen consists of two identical α1-chains and one α2-chain differing slightly in aminoacid-composition. From [6]

As shown in figure 2c, three α-chains can bind together, stabilised by hydrogen

intramolecular bonds, forming a right-handed coiled-coil triple helix. The type 1 collagen helix is heterotrimeric, composed of two α1-chains, and one α2-chain of similar amino-acid composition. They coil about the central axis in a one-residue staggered helical structure [7]. This unique helical conformation is possible because of the special composition of α-chains; the side chain of glycine being a hydrogen atom, is small enough to stereochemically fit inside the helix. The proline ring structures of the imino-acids stabilises the helical conformation of the chain. The chains are held together by the intramolecular hydrogen bonds between the amine-group of the glycine and the carbonyl-group of the adjacent peptide [8]. Figure 3 gives an overview of the synthesis and structure of collagen fibres. The procollagen is synthesized in the endoplasmatic reticulum and subjected to post-translational modification before it is secreted into the extracellular space. Peptidases in the extracellular space cleave both non-helical ends of the procollagen, yielding a tropocollagen monomer that is about 300nm long and 1.5nm wide [7].
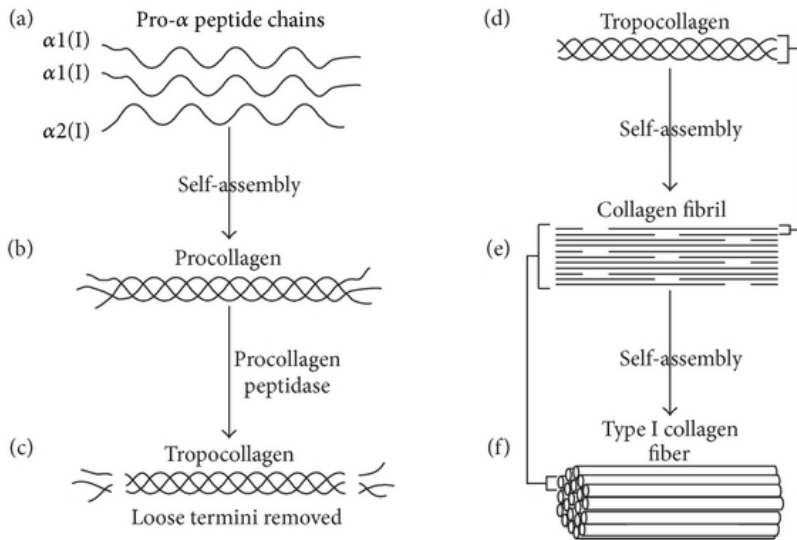
Figure 3: Schematic illustration of the process of collagen self-assembly. a) The three α-chains composing the procollagen, b) the procollagen triple helix with non helical termini, c) the proteolysed tropocollagen, d) self-assembly of tropocollagen into a staggered array, e) the collagen fibrils, f) collagen fibre. From [9]

4

Once the tropocollagen monomers have been trimmed of their non-helical ends they are susceptible to interactions with other collagen molecules. Hydrogen bonding, hydrophobic interactions, and interchain cross-links stabilise the tropocollagen, causing aggregation of monomers based on an entropy-driven self-assembly [10]. The small aggregates will further associate, expanding both linearly an laterally into fibrils, a mechanism termed nucleation and growth. As seen in figure 3, the tropocollagen rods will laterally assemble in a staggered arrangement. There is a 64-67nm displacement between each row, and 35nm between successive molecules in a row. This creates repeating regions of overlap- and hole-zones, causing a banding pattern of low and high density. This axial banding pattern of 64-67nm is known as D-periodicity, and the overlap structure has proven essential for the high tensile strength of collagen [10]. The final collagen fibrils will range in diameter from approximately 15 nm to 500 nm or more depending on the tissue [11].

The fibrils can further assemble into bundles held together by covalent crosslinking creating the collagen fibres. Collagen fibres can range in sizes from 1-500 µm [11]. The crosslinking of fibrils is the cause of the high tensile and mechanical strength of the fibres. The cross-links are based on aldehyde formation and condensation of peptidyl-, lysine- and hydroxylysine residues catalysed by the enzyme lysyloxidase (LOX) [8]. The crosslinked fibres form structures that can resist high tensile forces, because they are organised into networks withstanding stress in multiple directions. The organisation of the collagen network depends on the gene expression of the secreting cell. These cells also interact with the produced collagen, affecting the dynamic disassembly/reassembly of fibres both mechanically by "tugging" them into place, and chemically by secreting other proteins that influence collagen organisation [10].

Collagens rods can be extracted from tissues and dissolved in an acidic solution with weak ionic strength kept at low temperatures. These conditions prevent the tropocollagen rods from associating, and they are dispersed in the solution in their native triple-helix conformation. Once the pH has been neutralised with a base and the temperature is elevated, fibrillogenesis is induced and the rods can re-aggregate [12]. Studies on collagen assembly *In vitro* have demonstrated that the fibres have the same axial periodicity as native fibrils, indicating that the fibrillation occurs by the same mechanism. *In vitro* collagen assembly is largely influenced by environmental factors such as temperature, pH and ionic strength [13]. It is an endothermic process promoted by heating, and reversed by cooling [11]. The assembly is entropy-driven, made thermodynamically favourable by a large positive

entropy contribution from the displacement of structured water surrounding the collagen molecules. Additionally, water-mediated hydrogen bonding between polar residues is a strong driving force. Ions, alcohol and other substances that influences hydrophobic interactions or direct hydrogen bonding between polar residues has been shown to alter the fibre assembly [13]. The dependence of fibril assembly on solution pH and ionic strength suggests that electrostatic interactions stabilises monomer affecting fibrillation.

1.1.2 Collagen in Cancer

The ECM network of macromolecules surrounding the cells has traditionally been considered to act passively as a physical scaffold for the embedded cells, providing support while permitting exchange of nutrients and waste. However, in recent years the ECMs biochemical and biophysical signalling has been shown to have an active and complex role in regulating cell behaviour [5]. In developmental biology, mechanical properties of the microenvironment has demonstrated to be an important determinant directing stem-cell differentiation and tissue-development [14]. Many of the processes governing embryonic development also regulate cancer development, supporting the concept that biomechanical forces of the tumour microenvironment influences tumour progression [15]. There is increasing evidence for that the bidirectional interaction between cancer cells and the imbalanced, deregulated and disorganised tumour stroma is associated with an increased malignancy in cancers [15–17].

Fibrosis is the excessive formation of fibrous tissue, which in a normal response to injury causes scarring in tissue-repair. Fibrosis can also be a pathological reaction in cancers, with abnormal accumulation of ECM proteins, responsible for the clinical presentation of a tumour as a "lump" [18]. This strong fibrotic reaction is termed desmoplasia, and is characterised by the formation of abundant collagenous stroma [16]. There are a number of underlying mechanisms responsible for the desmoplasmatic reaction. Tumour cells can cause the proliferation of myofibroblasts and fibroblasts, creating cancer associated fibroblasts (CAFs) which demonstrate an inappropriate ECM synthesis and degradation. CAFs have an increased expression and desposition of type I and III collagen, and increased degradation of type IV collagen [16]. The cancer cells and CAFs will aberrantly express ECM-modifying enzymes such as matrix metalloproteinases (MMPs) and lysosyl oxidase (LOX) [15]. MMPs promote growth, invasion and metastasis of the

carcinoma by catalysing proteolytic degradation of ECM, altering the cell–cell and cell–ECM interactions to promote migration and angiogenesis [19]. LOX on the other hand catalyses the crosslinking between collagen fibres, resulting in increased tissue tension. Fibroblasts with an over-expression of LOX showed an increased crosslinking of the matrix components, promoting growth and invasion of cells in studies by Fang et al. [17]. LOX and MMPs have opposing roles in healthy tissues, where they together generate a tightly regulated and dynamic microenvironment. With the lack of control typical of cancers these enzymes are abberantly expressed resulting in a deregulated, deviant ECM.
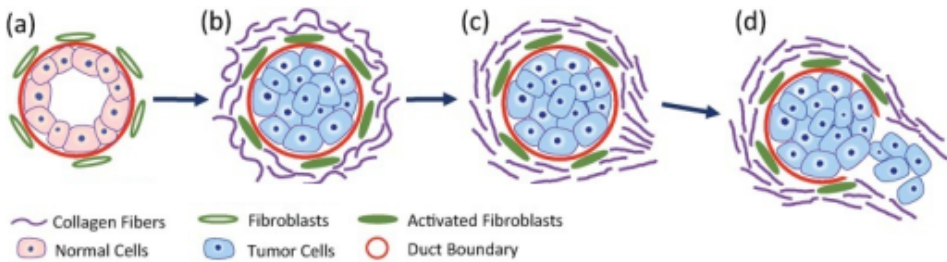

Figure 4: Schematic illustration of cancer progression in a mammary carcinoma. a) healthy milk duct, b)proliferation of tumour cells with a desmoplasmatic reaction, c) altered morphology of ECM with thicker and linearized collagen fibres, d) linear collagen fibres provide an "invasion highway" promoting metastasis. Figure adapted from [20].

The fibrillar collagen scaffold in cancer-associated stroma consists of thicker, linearised and stiffer fibres resulting from the elevated deposition of collagen from the CAFs, and the increased crosslinking of fibres. As illustrated in figure 4, regions high in deviant fibres creates a tumour invasion front shown to promote cell migration into the interstitial matrix and towards vasculature [18]. Studies by Provenzano et al. [21, 22] provided evidence that tumour-associated collagen is associated with increased malignancy and invasiveness of breast cancer.

The dense collagen network and increased stiffness of the ECM has in addition to elevated malignancy also been shown to induce chemoresistance of cancer. The delivery of anti-cancer-agents can be impeded by the desmoplastic stroma acting as a biological barrier. A tightly woven ECM-network can directly induce chemoresistance, as the small mesh size of the network can sterically prevent access of larger drugs [16]. The linear fibres are stiffer than native fibres, and contribute to the elevated interstitial fluid-pressure (IFP) of the TME, which hinders diffusion

of drugs into the tumour. Collagenase treatment on tumours has demonstrated to decrease IFP and enhance drug delivery [16]. Netti et al. [23] found that collagenase treatment on four types of penetration-resistant tumours significantly increased the diffusion rates. Loeffler et al. [24] reduced the number of CAFs in mice through vaccinating against fibroblast-activating protein expressed by CAFs. This resulted in reduction of type I collagen, with improved drug delivery and efficacy of chemotherapy in multidrug-resistant murine colon and breast carcinoma. Olive et al. [25] showed increased delivery and efficacy of chemotherapeutics after inhibition of Hedgehog signaling, reducing the demoplasmatic response in mouse model of pancreatic cancer.

1.2 Alginate

Alginate is a family of polysaccharides found as a structural component in cell walls of brown algae (*Phaeophycae*), which is where the molecule derives its name from [26]. The alginate provides mechanical strength and flexibility to the algeal tissue, by forming a gel with sodium, calcium, magnesium, strontium and barium ions [27]. Some soil bacteria, such as *Aztobacter vinelandii* and several *Pseudomonas* species, also produces alginates. These bacteria secrete the biopolymer as an extracellular polysaccharide, where it provides viscoelastic properties to the biofilm [27].

1.2.1 Chemistry and Structure

Alginate is a linear heteropolymer composed of two different monomers, β-D-mannuronic acid (M) and α-L-guluronic acid (G), linked by 1-4 glycosidic linkages as shown in figure 5. It is biosynthesised as a mannuronan homopolymer, upon which the enzyme mannuronan-C5-epimerase changes some of the M-residues into G-residues. The two resulting C-5 epimers adapt different conformations in spite of their similar chemical composition, resulting in widely different properties of the alginate molecule [27]. β-D-mannuronic acid adapts a $_4C^1$ ring conformation because it is more stable to have the bulky carboxyl-group in an equatorial position. When a C5-epimerase changes the carboxyl-group on the fifth carbon group to an axial position, the resulting guluronic acid is no longer stable in a $_4C^1$ conformation, but flips to a $_1C^4$ conformation to stabilise the carboxyl group in the equatorial plane once more. This flip results in different geometries of the 1-4 glycosidic linkages in the polymer. As illustrated in figure 5, this results in diequa-

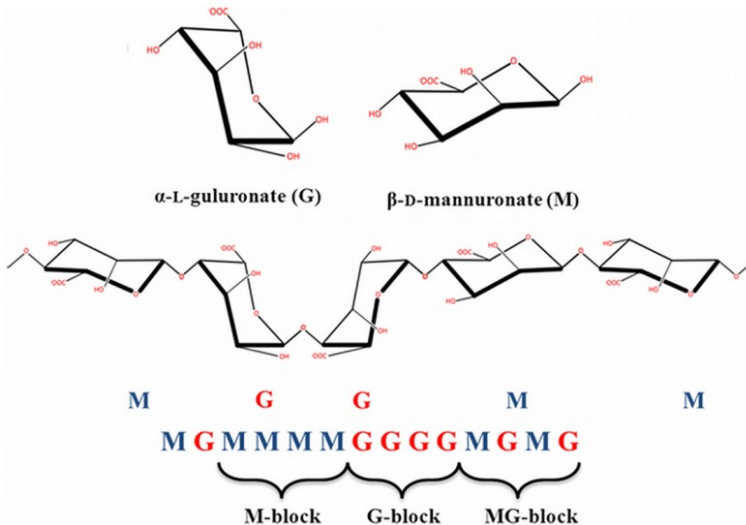torial M-M linkages, diaxial G-G-linkages, equatorial-axial M-G-linkages and axial equatorial G-M linkages.

Figure 5: Schematic illustration of the structure of the monomers of alginate, the C5-epimers α-L-guluronate and β-D-mannuronate. The difference in conformation of the two monomers, causes them to have different linking stereochemistry. This in turn causes homopolymeric "blocks" of the polymer to have different properties. From [28]

The type of linkages in the polymer chain is important for polymer properties, so the ratio of M- and G-residues and particularly the sequence of consecutive M- or G-residues is of interest. Alginate can be described as a block polymer, with 3 different constituents, homopolymeric blocks of consecutive M-residues (M-blocks), consecutive G-residues (G-blocks) or alternating M- and G-residues (MG-blocks). MG-blocks make the chain highly flexible because of rotations on the M-G linkage. M-blocks adapt an extended, flat, ribbon-like chain-conformation, while G-blocks form a rigid buckled chain. Alginate from different natural sources differ in the M/G-ratio, and the length of the blocks. The stipe of *L.hyperborea* has a high fraction of G-residues, with G-block stretches on average 15 monomers long. Alginate from *A. nodosum* on the other hand, is characterised by low G-block content. Purification enables obtaining only alginate chains of the desired composition and sequence of G-block [27].

Increasing molecular weight of polymers yields more viscous solutions, and gen-

erally results in stronger gels. Sodium alginates are commercially available in molecular weight range between 32,000 and 400,000 g/mol [29]. By acid hydrolisis the high molecular weight compounds can be degraded into molecules of lower molecular weights. Like other polysaccharides, alginates are polydisperse, with naturally derived samples containing a mixture of molecules of varying weights. The average molecular weight of the sample can be calculated in different ways, usually as number-average molecular weight (M_n), or weight-average molecular weight (M_w). The averages are defines in equations 1 and 2 where N_i is the number of molecules with molecular weight M_i, and w_i is weight of the molecule i.

$$M_n = \frac{\sum N_i M_i}{\sum N_i} \tag{1}$$

$$M_w = \frac{\sum w_i M_i}{\sum w_i} = \frac{\sum N_i M_i^2}{\sum N_i} \tag{2}$$

The average number of monomers per chain can be similarly denoted as the number- or weight-average degree of polymerisation (DP_n, DP_w). The DP- averages are defined equation 3, with M_0 being the molecular weight of a single monosaccharide of the biopolymer, and (M_n) or (M_w) being the number-average- or weight-average molecular weight, respectively.

$$DP_{n,w} = \frac{\sum M_{n,w}}{\sum M_0} \tag{3}$$

The exact composition and sequence of the biopolymer can be determined by nuclear magnetic ressonance (NMR), distinguishing between the monomers based on the quantum mechanical properties of the nuclei. NMR allows for exact determination of the fraction of guluronic acid and munnuranic acid monomers (F_G and F_M), and their sequence in the polymer. NMR is performed on samples that are partially hydrolyzed to DP< 50 to reduce the viscosity. High-performance anion-exchange chromatography with pulsed amperometric detection (HPAEC-PAD) can separate compounds based on the amount of negative charges, and will therefore efficiently separate different chain lengths of the anionic alginate. HPAEC-PAD suffers from poor resolution at long polymer chain lengths. Another approach is size-exclusion chromatography combined with on-line multi-angle laser-light scattering (SEC-MALLS), determining molecular weights based on differences in hydrodynamic volume.

1.2.2 Applications

Because of their interesting properties, alginates are of industrial importance, and approximately 30.000 tons are produced annually worldwide [27]. Most commercial alginates are produced from brown seaweeds, mainly *Laminaria hyperborea, Laminaria digitata* and *Ascophyllum nodosum*. Alginate from different biological sources may differ widely in properties, because each species synthesises alginate of different chemical composition and sequence of residues. In addition to species, different parts of the plant and season and growth conditions influence the polymer composition [27]. Alginates with a tailored block composition can be obtained by modifying with a mannuronan-C-5 epimerase produced by *Azotobacter vinelandii*

There is a wide array of uses for alginates, with most commercial applications being for their gelling ability upon addition of divalent cations such as Ca^{2+}. Alginates are commonly used as thickening agents, gelling agents, dispersion stabilisers, texturisers, filament or film formers [27]. In addition to this, alginate has been shown to be both biocompatible and biodegradable, making it a good material for medical- and food applications. In food industry it is used to improve the texture and stability of food products. In pharmaceutical industry it has traditionally been used for wound dressings and dental impression material, but more recently it has also been used for drug delivery systems, cell encapsulation, tissue engineering purposes, and against acid reflux [29].

1.2.3 G-blocks

Homopolymeric guluronate oligomers or "G-blocks" of specific chain-lengths can be synthesised by acid hydrolysis from composite alginates. The G-G glycosidic linkage is less susceptible to acid hydrolysis than M-M linkages because of their more protected conformation. This enables isolation and purification of short G-block oligomers from the alginate polymers by exploiting their acid solubility properties[30].

As described previously, G-blocks have a large influence on the mechanical properties of an alginate gel. G-blocks will selectively bind divalent cations such as Ca^{2+} in the cavity between the diaxial GG-linkage as illustrated in figure 6. The G-blocks can then form junction zones with an adjacent G-block through the ionic crosslinking agent (Ca^{2+}) in what Grant et al. [31] termed the "egg-box"-model. This crosslinking will only occur when the G-blocks are over a certain size, typ-

ically 8 or more consecutive guluronate molecules. In a composite alginate the G-blocks can aggregate whilst the M-blocks of the chain are still water soluble and flexible, creating a hydrogel. The viscosity and elasticity of the hydrogel thus depends on the ratio of M/G monomers (or fraction of guluronate monomers (F_G)), the length of the G-blocks as well as the molecular weight of the polymers [27].
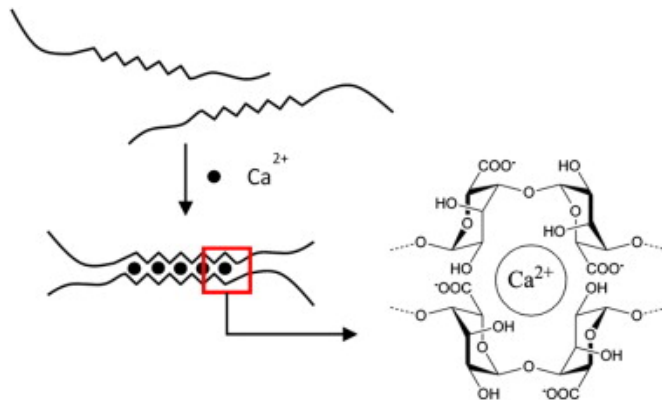

Figure 6: Illustration of the egg-box model of alginate gelation proposed by Grant et al. [31]. The divalent cation Ca^{2+} is selectively bound and stabilised by the hydroxy- and carboxyl groups in the GG-cavities. Junction zones between G-blocks on adjacent alginates form a gel-network. From [32]

G-blocks are preferred over MG-blocks and M-blocks in medical applications as they are generally non-immunogenic. In a study from Otterlei et al. [33] low molecular weight G-blocks has been shown to not induce cytokine production from human monocytes. Isolated G-block fragments have been investigated by Nordgård et al. [34] for their properties to influence barrier properties of the mucosal matrix, showing improved nanoparticle mobility in mucus and improved cellular uptake of nanoparticles through a mucus layer. Vitko et al. [35] showed that guluronate oligomers improves intestinal transit and survival in Cystic fibrosis mice by reducing the accumulation of intestinal mucus.

1.2.4 Rixova

Rixova is a new drug candidate based on G-blocks developed by Professor Kurt I. Draget and Dr. Catherine T. Nordgård. It has demonstrated to reduce growth in mouse models of pancreatic cancer both as a single agent and in combination

with standard chemotherapy gematicine [36]. However, the mechanism of action is not fully understood. It is suggested that the G-blocks are able to modulate the structure of the ECM based on their electrostatic interaction with type 1 collagen. The G-blocks are possibly masking regions of the collagen fibres, hindering them from interacting with other fibres and thereby reducing the crosslinking in the network. Reduced density of the ECM matrix might ease the diffusion of anti-cancer drugs into the tumour, or the altered cell-ECM interactions may in themselves be enough to normalise the tumour microenvironment.

2   Aim of Thesis

This thesis investigates the influence of guluronate oligosaccharides (G-blocks) on the fibrillogenesis of type I collagen. As type I collagen is the main structural protein of the ECM, a demonstrated effect of G-block on collagen *in vitro* can help explain the mechanism behind the effect of Rixova on tumours that has been observed in clinical trials.

The aim of this thesis is to investigate both the structure of the collagen network, and the mobility of particles within it, upon treatment with G-blocks. The abnormal collagen architecture in cancers causes elevated tension of the tumour microenvironment and poor penetrability which has shown to increase malignancy and reduce delivery of chemotherapeutics. The development of these properties will be monitored from the moment G-block is added until the final collagen network is formed. This might provide additional information on G-blocks effect on the kinetics of collagen self-assembly and on the nature of the interaction between the two biopolymers.

3   Technical Introduction

To investigate the effects of alginate oligomers upon the structure of collagen matrices, multiple methods have been employed. Confocal reflectance microscopy was the main method for real-time visualisation of the developing network structure. Simple MATLAB-functions weer developed to analyse the fibre-dimensions. Spectrophotometry was applied to validate this method, by monitoring turbidity-development as a measure of fibril-formation. To investigate the mechanical properties of the developing collagen network multiple-particle tracking of fluorescent

particles suspended in the collagen solution was applied. Mean-square displacement of the particle-trajectories was analysed and used to inform on the microrheological properties of the network at different timepoints. The simultaneous microrheological measurements and non-invasive imaging of structure enabled a unique insight on the correlation between the collagen structures that are formed and the resulting mechanical properties of the gel.

3.1   Turbidity

Measuring turbidity has traditionally been the preferred method to investigate the kinetics of collagen fibrillogenesis [13, 37–39]. During fibril-formation the turbidity of the collagen solution increases, as it changes from a nearly transparent liquid of stabilised tropocollagen monomers, into light-scattering fibrils [40]. Both the size and the density of fibres affect the turbidity of the solution [38]. A spectrophotometer measuring the transmittance of light passing through the solution can be used to assess the turbidity of the sample [38].

Spectrophotometry is a method used to study a materials transmittance and reflectance of light as a function of wavelength [41]. The light applied can be absorbed or scattered by the molecules in the solution. Molecules in the solution only absorb photons at certain wavelengths called the molecules adsorption spectrum, photons of all other wavelengths are emitted. A spectrophotometer measures this transmitted light and calculates the amount of light absorbed by the analyte at this wavelength [38]. The basic setup of a spectrophotometer is illustrated in figure 7.

$$T = \frac{I}{I_0} \tag{4}$$

$$A = \log \frac{1}{T} = -\log \frac{I}{I_0} \tag{5}$$

The transmittance (T) of a solution is defined as the ratio of intensity of transmitted light (I) to the intensity of the incident light (I_0), as shown in equation 4. The amount of light absorbed by the sample(A) is inversely related to the amount of transmitted light by the relation shown in equation 5. The spectrophotometer calculates both the transmittance and absorbance of the solution at the specific wavelength.
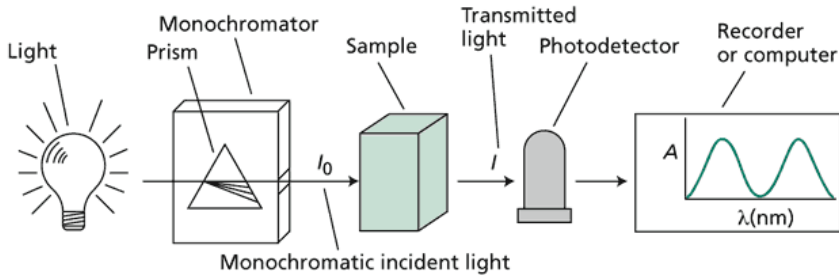
Figure 7: Diagram showing the main parts of a spectrophotometer. The monochromator/prism is set to produce a specific wavelength of light that passes through the sample. The intensity of this incident light is denoted as I_0. The light that is not absorbed, but passes through the sample is called the transmitted light. The intensity of the transmitted light, I, is detected by a photodetector. The calculated absorbance is recorded on the computer as a function of wavelength. From [41]

$$A = \varepsilon \cdot l \cdot c \tag{6}$$

$$\tau = \frac{A}{l} \ln 10 \tag{7}$$

Following Beer-Lamberts law, the relation between the absorptive capacity of the analyte and the concentration of analyte is described by equation 6. Here c is the solute concentration, l is the pathlength of the light through the cuvette (cm), and ε is a constant for the molar absorptivity. The turbidity of a solution is a measure of the intensity decrease of transmitted light due to scattering. In fibrilllogenesis the analyte-concentration causing turbidity is the mass of collagen present in fibril form, since solubilised monomeric tropocollagen are of to diameters to small to scatter light [39]. Assuming that collagen fibres are randomly oriented, rigid rod-like and monodisperse, the relation between turbidity τ and absorbance shown in equation 7 has been derived from Beer-Lamberts law, with A and l again being the absorbance and optical pathlength respectively. This relation has shown experimentally to be a good approximation for collagen fibres [38].

As illustrated in figure 8, the turbidity-time curves of collagen fibrillation typically grow in a sigmoidal fashion consisting of a lag-phase and a growth phase until it reaches a plateau of maximum turbidity. In the lag-phase smaller aggregates appear, but these are yet to small to scatter light. Later in the growth phase
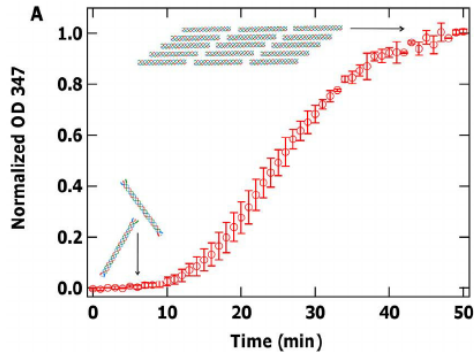
Figure 8: Illustration of the typical turbidity-time curve in a collagen fibrilliation process. In the lag-phase small aggregates are formed that do not scatter light, in the growth phase linear and lateral growth of the initial aggregates causes rapid turbidity growth of the solution. Figure adapted from [42]

these aggregates grow into fibres large enough to scatter light, leading to a rapid increase in turbidity of the solution. Both the number of fibres and their sizes contributes to the turbidity of the sample. Finally, the turbidity-time-curve reaches the plateau-phase where the turbidity stops rising, although this does not mean that the fibre-network remains constant [40, 42].

3.2   Confocal Reflectance Microscopy

Confocal reflectance microscopy (CRM) is an optical imaging technique that can be used to study the structure of the collagen matrices [37]. The goal with this imaging is a qualitative and quantitative evaluation of the structural parameters and organization of the fibre network. Combining reflectance imaging with confocal microscopy, enables optical slicing of the specimen without staining or processing [37]. The non-invasiveness of the procedure allows for real-time-visualisation of fibre-developement, providing both structural and kinetic information. Turbidity has traditionally been used to study the kinetics of collagen fibrillogenesis, but this method does not provide accurate information on fibre number and sizes, and does not show fibre connections. The resolution on CRM is significantly lower than other microscopy methods such as scanning electron microscopy (SEM). However, the advantage of CRM is that the non-invasiveness of the imaging allows for simple and accurate 3D evaluation, and timelapse-visualisation of the developing network.

3.2.1 Reflectance

CRM takes advantage of the fact that collagen fibres with a diameter over 500nm reflect light [40]. For a material to give a good reflection contrast it needs to have a high reflectance or albedo, or show a significant index-of-refraction at its boundaries [37]. The coiled collagen fibres differ substantially in refractive index from a surrounding media like water. Since the backscattering of light is an intrinsical optical property of collagen, there is no need for any prior staining of the sample, and it can be visualized as is.

3.2.2 Confocal Microscopy

Contrary to wide-field microscopy, where the entire specimen is flooded in light, a confocal microscope uses point illumination. Light from the laser is focused on a small focal point on the sample as illustrated in figure 9, and by using a scanning laser the different spots of the sample are illuminated in turn so that an entire image can be regenerated. The reflected light is propagated back to the objective lens that focuses it into a spatial pinhole filter. The pinhole has a diameter of aperture same as the diameter of the optical slice. Light from the illuminated spot in the correct focal plane is admitted, but light returning from out of focus planes is filtered out. This makes it possible to only view a thin vertical plane of interest, and mask out the planes above and below. This technique of imaging at a specific depth of the specimen is termed optical sectioning [43].

The reflected light admitted through the pinhole is detected by a photomultiplier tube (PMT). These detectors are highly sensitive, and can multiply the incident light to give a stronger signal. The depth at which the objective lens focuses in the z-plane can be changed. This enables obtaining a series of images at different depths, a z-stack. This optical slicing is a noninvasive method to observe different focal planes along the z-axis and reconstruct a three-dimensional image, all without the need for sample-manipulation. The 3D-image has poorer resolution in z-direction, as the z-stack cannot be as finely-sliced as the xy-plane is resolved. Since the method is non-invasive it can also be used to measure the same spot in the centre of a specimen over a period of time, yielding a time-series of images as demonstrated by Brightman et al. [37].
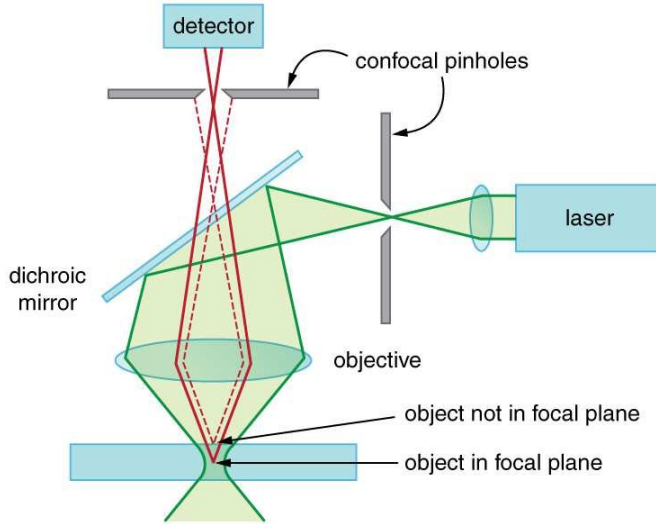
Figure 9: Schematic illustration of the basic components of a confocal microscope. The light emitted from the lasers passes through the excitation apperature, and is focused onto the specimen by the objective lens. All parts of the sample illuminated by the excitation light will reflect light back through the dichromatic mirror. Only the in-focus light emitted from parts of the sample in the correct focal plane is admitted through the pinhole aperture and enters the detector. From [44]

3.3 Multiple Particle Tracking

Multiple particle tracking (MPT) is an analytical technique that allows measurement of particle mobility in a solution. It is a high throughput method of single-particle tracking (SPT), where analysing the motion pattern of multiple particles provides information on overall particle-environment interactions. This information can be used to describe properties of the surrounding material, such as viscoelasticity, pore-size, or microrheology within pores [45].

Microscopic motion of multiple particles is monitored real-time using video microscopy. The short time-scale and high framerate of the video is essential to capture the rapid microscopical motion of the particles. The concept of timescale in MPT is illustrated in figure 10. In this example the framerate is 30 frames/s, yielding a minimum timescale of 33ms. Taking a freely diffusing particle as an example, the particle displacement on the shortest timescale (from one frame to the next) is on average quite small as the particle does not have time to move

much in the 33ms between frames. The displacements between frame 1-2, 2-3 and 3-4 etc is averaged to give a time-average displacement for the time-scale. Looking at a larger time-scale such as 330ms, measuring the displacement between every ten frames, the time-average displacement from the reference state is likely to be larger, as the particle has more time to diffuse. This time-scale-dependent variance in particle displacement informs on the type of motion of the particles [46].
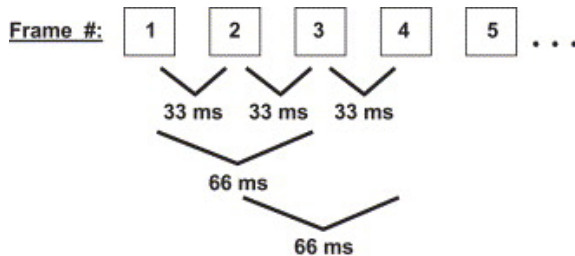

Figure 10: Illustration of the concept of timescale in multiple particle tracking. From [45].

The video-recording of particle-movement is analysed with suitable software to obtain the x- and y-positions of the individual particles, and their trajectories over time can be plotted. This positional data allows for the calculation of the mean-square displacement (MSD), a measure of the deviation from reference position within a timescale [47].

3.3.1 Mean-Square Displacement

For a particle trajectory tracked in two dimensions, MSD is calculated by equation 8, by combining the average displacement in each dimension (Δx^2 and Δy^2). In equation 9 the positional change in each dimension is described as a function of time (t) and timescale (τ). Here $x(t)$ and $y(t)$ are the x- and y-coordinates of the particle at time (t). τ is the timescale meaning the lag-time between the two frames chosen, as ascribed in the previous section. The angular brackets $< ... >$ indicate the average of various initial times (t) from each trajectory.

$$MSD = < \Delta r^2(\tau) > = < \Delta x^2 + \Delta y^2 > \tag{8}$$

$$\begin{aligned} < \Delta x^2 > &= [x(t+\tau) - x(t)] \\ < \Delta y^2 > &= [y(t+\tau) - y(t)] \end{aligned} \tag{9}$$

19

For multiple-particle tracking, the ensembles average of trajectories can be obtained as shown in equation 10. This is useful for studying the mobility of the entire population of particles, which provides information on the mean material properties of the surroundings. Here the double angular brackets $<< ... >>$ indicate the ensemble-average time-average displacement of particles.

$$< MSD >=<< \Delta r^2(\tau) >> \tag{10}$$
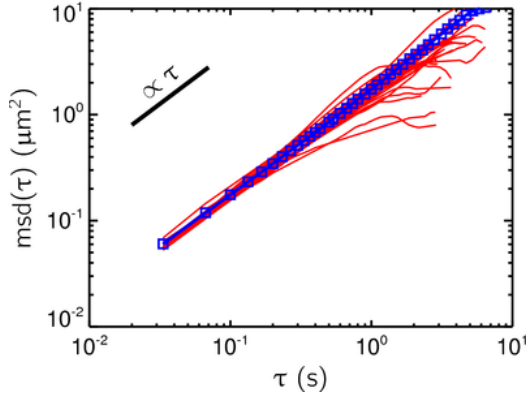
Figure 11: MSD as a function of timescale is plotted for multiple particles shown as red lines. The blue points are the calculated time and ensemble averages for all trajectories. The black line indicates the linear scaling of MSD$(\tau) \propto \tau$. From [48]

In figure 11 MSD as a function of time-scale (τ) is calculated for multiple particle trajectories. Each red line represent the time-average MSD of one particle, the blue line represents the ensemble-average time-average MSD of all the particles. As seen from this graph, the MSD of all the particles grow linearly with increasing time-scale. This is typical for Brownian-motion pattern for particles in a continuum viscous material, that allows for unhindered diffusion [47]. If the surrounding material is not a Newtonian fluid, the MSD response is not linearly scaled to the lag-time. This can be used to identify the mechanical properties of the surrounding material [45].

$$MSD = \tau^\alpha \times \Gamma \tag{11}$$

$$log(MSD) = \alpha \times log(\tau) + log(\Gamma) \tag{12}$$

20

Fitting $\log(\text{MSD})$ and $\log(\tau)$ to a straight line yields the slope of the line, the anomalous exponent (α) described in function 11 and 12. As stated previously, an anomalous exponent of $\alpha = 1$ where $\text{MSD}(\tau) \propto \tau$ indicates that the particles move by Brownian-motion in an unhinderd manner. For $\alpha > 1$, the particles are demonstrating anomalous superdiffusion by active transport or drift in the sample. For $\alpha < 1$, particles display anomalous subdiffusive motion, exhibiting restricted motion since the surrounding medium is confining their motility. The different types of anomalous diffusion is illustrated in figure 12.
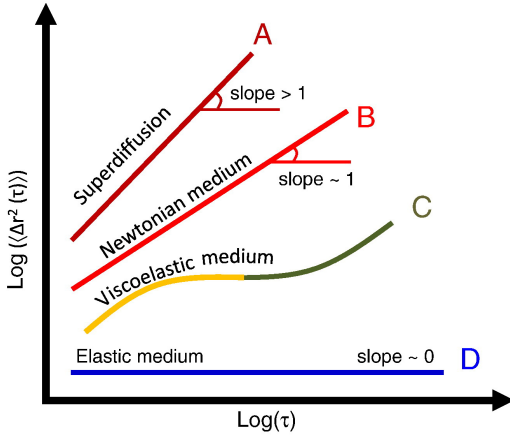
Figure 12: Logarithmic plot of MSD as a function of timescale (τ) for particles in different medium. A = Superdiffusive motion (active transport), B = Newtonian medium (Brownian motion), C = Viscoelastic medium, D = Elastic medium. From [49]

3.3.2 Microrheology

Analysing the MSD of suspended particles informs on the materials microrheology, the deformation of flow in a tiny volume of the sample. In contrast to macro-scale rheology measuring properties of the bulk fluid, microrheology measures the viscoelasticity of micro- and nanoscale components. For a heterogeneous system, such as a gel containing elastic fibres and low viscosity fluids, microrheology allows for characterisation of the local environments. This means measuring the fluid within the biopolymer network as well as the network mesh itself. Macrorheological characterisation of the same heterogeneous system measures the bulk fluid properties, averaging the viscoelastic properties of the whole system rather than measuring

the individual micro-scale components.

Since MSD analysis of MPT measures the local environment it is well suited for monitoring the sol-gel transition. As demonstrated by Moschakis [49], the MSD of particles in the solution can be followed at different moments in the course of gelation. When the solution is fluid(sol-state) the particles can diffuse freely, exhibiting Brownian-motion, as seen in figure 13a. When a gel is formed with a network mesh size comparable to particle-sizes, the particles become restricted in their motion. In figure 13b some individual sub-populations amongst the particles can be observed, some with highly confined motion, while others display a free motion pattern. This difference could not be detected by macrorheological measurements, and is typical of a heterogeneous systems such as a gel with some particles diffusing freely within a pore, and some more constricted by tighter junctions of the network [49]. The fibre-network hinder the free movement, and there is an elastic coupling between particles and network. When the sol-gel transition has completed, a dense fibre-network will lead to full confinement of the particles, and the elastic coupling between particles and network lowers the α-value. The MSD does not increase at longer time-scales, giving an anomalous exponent of $\alpha=0$ as seen in figure 13c.

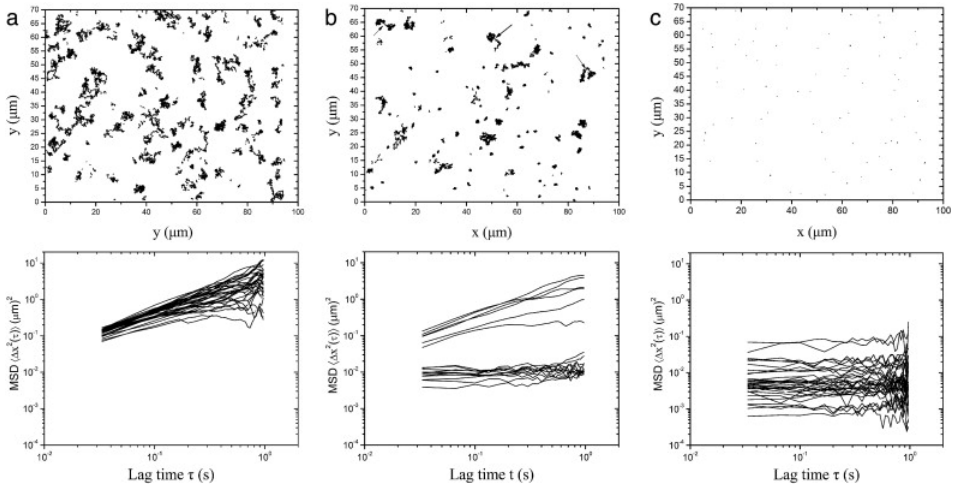Figure 13: Logarithmic plots of MSD as a function of timescale τ at different timepoints of gelation a) before gelation, b) during gelation, c) a long while after gelation. From [49]

4   Materials and Methods

4.1   Materials

4.1.1   Collagen

The collagen used for all experiments is Corning® type I, rat tail collagen in powdered form. The manufacturer obtained the tropocollagen monomers by extraction into 0.5 M acetic acid and filtering (0.2 µm membrane), no enzyme digestion steps are used so that the helical ends of the tropocollagen monomers are still intact. For use in this experiment the powder is dissolved in 0.1% acetic acid (HAc) to a 5mg/ml concentration. All gels have a final concentration of 2mg/ml collagen.

4.1.2   Alginates (G-blocks)

All alginates used are listed in table 1. The samples are prepared by acid precipitation of high molecular weight alginates. Alginate G-block DPn-24 is purified from alginate sample "G-blokk H3", alginate G-block DPn-33 is purified from alginate sample "G-blokk Batch801-255-02", both a gift to Professor Kurt I. Draget from FMC Biopolymer AS (Drammen, Norway). Alginate DPn-12 is produced by acid hydrolysis of "G-blokk H3". Alginate M-block is purified from high F_M-sample from *Macrocystis*, the manufacturer of this alginate was not listed.

Table 1: Alginate samples used to modify type I collagen. G-blocks are prepared by Camilla M Reehorst (CMR), M-block is prepared by Ingrid Aune(IA). Average degree of polymerisation (DPn) and fraction of guluronate monomers (F_G) for the samples is provided by their original producers. * indicates the DPn found in this experiment.

Alginate	DPn (HPAEC-PAD)	DPn (NMR)	F_G	Date	By
G-block DPn-12	12 (11.8*)	12	0.932	08/9-13	CMR
G-block DPn-24	24	24.5	0.899	30/8-13	CMR
G-block DPn-33	33	36	0.868	30/8-13	CMR
M-block DPn-20	20	-	0.17	14/1-97	IA

All samples of G-blocks are prepared by Camilla M Reehorst. She provided the number-average degree of polymerisation (DPn) determined by NMR and by

HPAEC-PAD (Dionex BioLC System, Dionex Corporation, Sunnyval, Ca), and the F_G found by NMR. HPAEC-PAD in this study found a more accurate DPn=11.8 for the DPn-12 sample, but determination of DPn was not possible for high Mw samples because of poor resolution in the chromatogram for larger molecules (full chromatograms are given in appendix A.1 and A.2). The NMR and HPAEC-PAD methods disagree on the average chain length of the alginate molecules. The NMR results are chosen for nomenclature throughout this thesis, as they are thought to be more reliable than HPAEC-PAD which suffers from poor resolution at long polymer chain lengths. The M-block sample is prepared by Ingrid Aune, with the DPn and F_G determined by NMR.

4.1.3 DPBS

HyClone^{TM} Dulbecco's phosphate-buffered saline (DPBS) 10x is prepared to a 1:10 dilution with Milli-Q (MQ) filtered and deionized water. The buffer contains no calcium or magnesium, and has a pH range 7.0-7.6, and osmolality 2.76 ± 0.01mOsm/kg H_2O.

4.1.4 NaHCO$_3$

Sodium bicarbonate manufactured by Sigma Aldrich^{TM} is dissolved in MQ water to a 7.5%(w/w) concentration (7.5g/100ml). Final concentration of NaHCO$_3$ in gels is 0.35mg/ml.

4.1.5 FluoSpheres

For MPT the fluorescent particles Invitrogen^{TM} FluoSpheres$^{\circledR}$ are used. They are 0.5 μm diameter polystyrene microspheres beads with a carboxylated coupling surface. The particles are loaded with yellow-green fluorescent dye (Ex/Em = 505/515). The 2% solids solution was diluted in buffer so that the final gel contains 0.0002% solids.

4.2 Methods
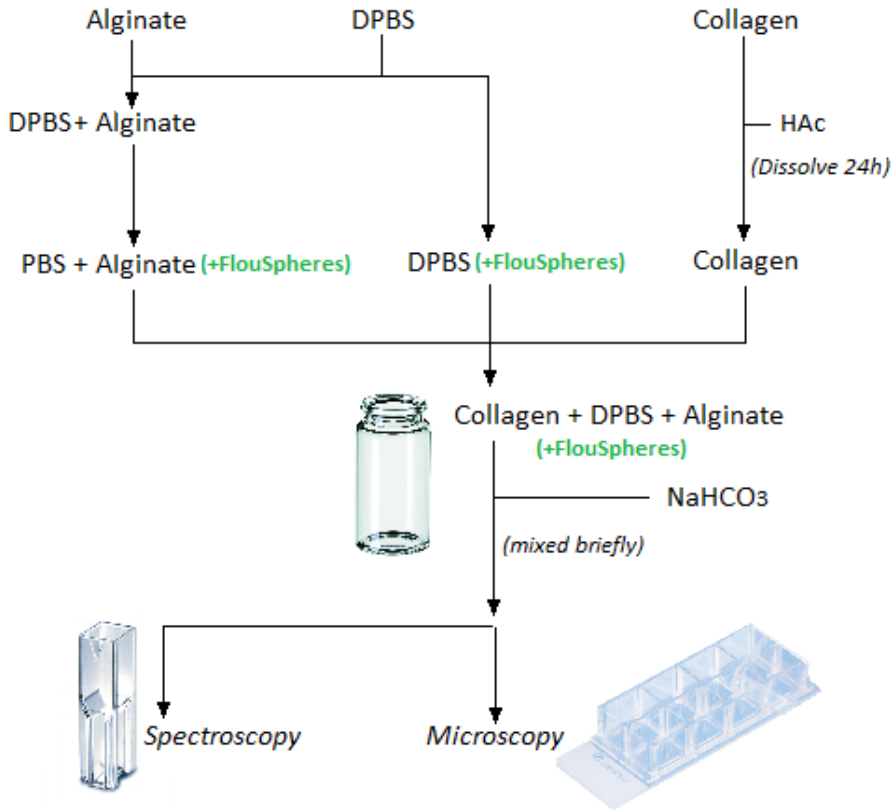
Figure 14: Schematic overview of the protocol for mixing collagen gels with different concentrations and compositions of alginate. FluoSpheres were only added in samples for MPT-analysis.

4.2.1 Collagen gel

Gelation is initiated by neutralising the pH of the collagen sample with addition of NaHCO$_3$, and increasing temperature. All materials are prepared in a 4 °C cooler to ensure the gelation does not take place prematurely. All equipment and containers are kept in the cooler at least 10 min prior to use to ensure minimal heat-transfer. If the gel is to be investigated at gel-equilibrium, the sample is incubated overnight at 40 °C. For turbidity or time-lapse CRM, NaHCO$_3$ is added

in close proximity to the spectrophotometer or microscope to ensure minimum time-delay before the first measurements of gelation. An overview of the protocol is given in figure 14, table 2 shows the measurements for making collagen gels with varying G-block concentration.

Protocol for collagen gels

1. 2000 µL of acetic acid (HAc 0.1%) is added to the vial of 10mg collagen, to a final collagen concentration of 5mg/mL. The solution is left to swell and dissolve for a minimum of 24 hours.

2. The collagen is stirred well with a spatula to ensure a homogeneous solution, taking care not to introduce any airbubbles.

3. 400 µL of the collagen solution is transferred to a chilled glass vial.

4. 555 µL DPBS 1:10 is added to the vial . The DPBS contains dissolved alginates and fluospheres if the sample requires.

   - G-blocks and M-blocks are weighed and dissolved into the buffer to a 9mg/ml concentration yielding a maximum 0.5mg/ml final concentraion in the gel. (For the extra high G-block-concentration experiment 14.40mg/ml alginate was used yielding an 8mg/ml final concentration in the gel.)

   - The 2% (w/w) fluoSpheres in stock solution was briefly vortexed and diluted 1:5555 in the buffer-solutions. This gives a concentration of 0.00036% (w/w) solids in both pure buffer and buffer with G-block, giving a final gel-concentration of 0.0002% (w/w).

   For lower concentrations of alginate, the high concentration stock is diluted with pure DPBS 1:10 as shown in table 2.

5. 47 µL 7.5% NaHCO$_3$ is added, neutralizing the solution and initiating the gelation.

6. The mixture is briefly stirred, taking care to not introduce any airbubbles, before transferring 800 µL to cuvette for spectroscopy or 300 µL to the wells on coverglass for microscopy.

All samples contain 2mg/ml type I collagen and varying alginate concentration. Usually the final concentration of alginate is 0.05mg/ml or 0.5mg/ml as shown in table 1 yielding w/w ratios alginate:collagen of 1:40 and 1:4 respectively. High

concentration samples with 8mg/ml G-block DPn-12 was prepared for one experiment, with alginate:collagen w/w-ratio 4:1.

Table 2: The measurements used for mixing collagen gels with varying concentration of alginates (G-blocks).

Sample	Collagen (5mg/mL)	DPBS 1:10	DPBS 1:10 G-block (9mg/mL)	NaHCO$_3$ 7.5% (w/w)
No added G-block	400 µL	555 µL	-	47 µL
0.05 mg/mL G-block	400 µL	500 µL	55 µL	47 µL
0.5 mg/mL G-block	400 µL	-	555 µL	47 µL

4.2.2 Turbidity

Turbidity of collagen gels is monitored at 400nm in a UV-16000 PC Spectrophotometer from VWR. Absorbance is measured every 10s for up to 3h. Samples are kept in a 1cm Brand UV microcuvette with a chamber volume of 70-850 µL. All solutions are prepared in a cold room (4 °C), and transferred to a spectrophotometer at room temperature (25 °C). Measurements start within 1 min of neutralisation.

4.2.3 Microscope Setup

All imaging is performed with a confocal microscope Leica TCS SP8 using reflection- and fluorescence imaging. The gels are monitored directly in LabTek® chambered borosilicate coverglass system. The microscope is a Leica DMI 6000 CS AFC Bino inverted microscope. The objective used is a HCX IRApo 25x/1.95, water-immersion objective. Images with a physical size 232.5x232.5 µm are acquired in the centre of the gel, approximately 500 µm from the slide, with motorised XY-stage and super z-galvo stage focusdrive. White Light Laser (WLL) with a wavelength range of 470-670nm is set to 488nm with 70% intensity. The internal detectors used are PMT (standard photomultiplier tube) for reflectance imaging, and HyD (GaAsP detector) for fluorescence imaging. In detail description of microscope-settings is given in table 3 and the full settings are given in appendices.

Incubation temperature is controlled via heating with a large incubator covering the entire microscope, for warm air incubation and CO$_2$-control (The Cube and

The Box from Life Imaging Services). Temperature is preset to 37 °C 1-2 hours before sample imaging to ensure a stable heating.

The software used is Leica LAS AF version 3.1.2. with the Live data mode (LDM) software model. The LDM tool allows for a predefined experiment ("pattern") to be set up composed of multiple time-lapses ("jobs") as shown in figure 15. A pattern was made with a reflectance image followed by a 20s time-series of fluorescence images. With a 54s pause the total loop becomes 2.5min long with 36 loops giving a total duration of 90 min for the whole pattern.
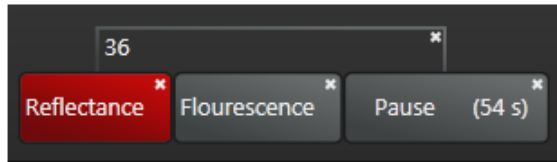

Figure 15: Live Data Mode pattern used to obtain the time-lapses. A dual job with reflectance- and florescence imaging was created, to perform simultaneous TL-CRM and a time-series of MPT-videos. Gels were monitored for 1h 30min, with imaging every 2.5min requiring 36 iterations of the loop.

Reflectance imaging is used for structure analysis, and settings are adjusted to yield a single high-resolution image. Florescence imaging is used to record a time-series with a high frame rate of 714ms (28 images in 20s), meaning that the resolution is necessarily lower, but enough to track the florescent particles. Table 3 provides a comparison of the different settings for microscopy in reflection- and florescence mode. Representative scan settings for reflection mode is given in appendix B.1. Representative scan setting for florescence mode is given in appendix B.2.

4.2.4   Image Analysis for CRM

To analyse the images obtained by confocal reflectance microscopy multiple software are used. LAS X is used as the built-in software of Leica SP8, Fiji (ImageJ) is used for image processing and MATLAB is used for data-analysis and as a graphing-tool. An overview of the image processing is given in figure 16.

The images obtained by reflection-microscopy are saved as .lif files and viewed in LAS X software (figure 16a). Images are exported with loss-less compression as .tiff files for further image-analysis in Fiji (ImageJ). Fiji is a distribution platform

Table 3: A comparision of the settings used for reflection- and fluorescence mode imaging. Full settings listed in apendix.

	Reflection	**Fluorescence**
Pixel sixe	0.104 µm	0.455 µm
Logical size	2232 pixels	512 pixels
Scan mode	xyz, z: 0	xyt, t: 28
Frames	36	1008
Scan speed	100Hz	700Hz
LineAverage	3	1
Laser	WLL, 70% power	WLL, 70% power
Laser line	488nm Intensity: 4.6223%	488nm Intensity: 6.3741%
Detector	PMT(459nm-561nm) Gain: 772.2	Hyd(485nm-497nm) Gain: 121

for ImageJ an open source Java image processing program. It comes with many plugins useful for scientific image analysis in fields such as life sciences [50]. In ImageJ the scale of the images is set, and canvas size is adjusted to 500x500 pixels. One of the corners of the image was selected as the new cropped image, so as to circumvent the central reflection from the microscope apperature as shown in figure 16b.

Ten horizontal lines are selected by using ROI-manager allowing simultaneous measurement of multiple regions of interest. The same ROI-lines were used for all measurements throughout the project. The pixel-intensities of the selected ROIs are measured using the multiplot function which plots the intensity-profiles of all 10 lines. The pixelintesity-values can be obtained as a list, with X0 describing the length along the x-axis of the image, and Y-values the pixelintesity at each distance as shown in figure 16c. The xy-table is exported as a .csv-file.

The pixelintensity-values are imported to MATLAB for fibre-analysis [51]. MATLAB is a scripting language used for numerical dataanalytics, developed by MathWorks [52]. To interpret the pixel-intensity data three functions for fibre-analysis were developed to detect a fibre and measure its size.

Num_peaks defines what is a fibre in a single ROI-line from the image, counting numbers of fibres and listing their diameters. A fibre is defined as having pixelin-

(a) LAS X

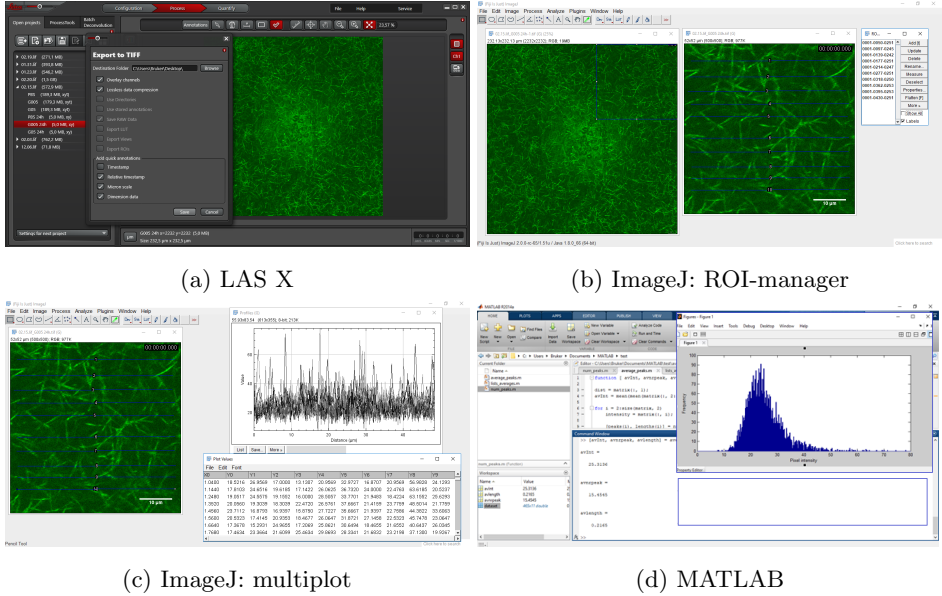(b) ImageJ: ROI-manager

(c) ImageJ: multiplot

(d) MATLAB

Figure 16: An overview of the software used for the processing of CRM-images. In a) images are exported from LAS X as .tiff with dimensional and time data and lossless compression. In b) the ROI-manager of imageJ is used to select 10 horizontal lines in the cropped image. In c) multiplot-function obtains profileplot of pixel-intesities along the ROI-lines. "List" provide the intensity values as a table. In d) MATLAB is used to analyze the intensity values to evaluate the fibres in the image. The functions developed for fibre-analysis are given in appendix C.

tensity over a certain "cutoff"-value that is based on the average intensity. The length of a high pixel-intensity-region thus corresponds to the diameter of that fibre. (Note that this function does not take into account that some fibres may lie horizontally along the selected ROI-line, resulting in abnormally large "diameters".) The MATLAB function is given in appendix C.1. *Average_peaks* finds the average number of fibres and average fibre-diameter of the ten lines in an single CRM image. The MATLAB function is given in appendix C.2. *List_peaks* is used for time-series analysis, when there are multiple CRM-images to be analyzed. The "cutoff"-value defining a fibre is calculated from the first image in the time-lapse. *List_peaks* provides a table of the fibre-analysis-values at each time-point, providing information in development of total pixel-intensity, fibre-number and average fibre-diameters. The MATLAB function is given in appendix C.3.

4.2.5 Mutliple Particle Tracking and MSD-analysis

MPT is achieved by adding fluorescent spheres to the solution, and monitoring their movement during the sol-gel transition of collagen. The videos from different time-points are imported to the image analysis software Fiji(ImageJ), where particles can be identified and tracked with the plugin ParticleTrackerJ an algorithm made by Sbalzarini and Koumoutsakos [53]. The coordinates of the particle-trajectories are imported to the analytical software MATLAB. In MATLAB the MSD of each trajectory is calculated and particle movement is analysed. An overview of the process is given in figure 17.
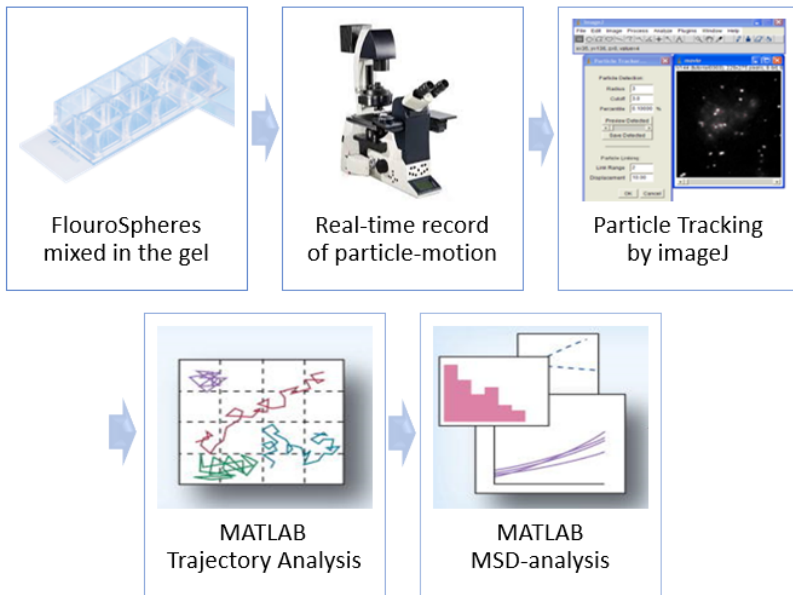
Figure 17: Schematic flowchart of the process for MPT and MSD-analysis. Fluorescent spheres are added to the solution, and particle movement is monitored real-time with the confocal microscope. In ImageJ the particles are located, and MATLAB allows for plotting and analysing their trajectories. Figure inspired by [45].

Fiji is as described previously a distribution platform for ImageJ an open source Java image processing program [54]. The imageJ plugin ParticleTrackerJ is a 2D and 3D feature point-tracking tool for the automated detection and tracking of particle trajectories. The algorithm is well suited for video imaging in cell biology

relying on low-intensity fluorescence microscopy [53]. The image-stack of a series of time-lapses is scaled, cropped and split into the respective time-lapses from each time-point. Each time-lapse is individually analysed with ParticleTrackerJ using the settings in table 4. The kernel size is set to a radius of 2 pixels (1 µm), to capture the 500nm particles. The cutoff is set low as there is an even distribution of particles. Percentile absolute intensity value determines which bright pixels are accepted as particles, and is set to 0.2% since the particle concentration is low. Displacement is the maximum number of pixels a particle is allowed to move between two succeeding frames, and the dynamic link is the number of subsequent frames that is taken into account to determine the optimal correspondence matching [53]. All the trajectories are gathered in a table saved as a .csv file.

Table 4: Settings applied for the ImageJ plugin Particle Tracker.

Parameter	
Radius	2 pixels
Cutoff (0-1)	0.001 pixels
Per/Abs	0.2%
Link Range	2 frames
Displacement	10 pixels
Dyanmics	Brownian motion

The trajectory data from ParticleTrackerJ is imported into MATLAB. For the MSD-analysis the MATLAB per-value class "@msdanalyzer" developed by Tarantino et al. [55] was employed. The @msdanalyzer performs automatic computation of multiple particle trajectories, with built in tools for plotting and inspecting data. To use the MATLAB per-value class, three functions have been developed. *Make-Cell* converts the ParticleTrackerJ -trajectories from a matrix to a cell fitting the predefined class of @msdanalyzer (appendix D.1). *MSDanalyzer* is developed for a quick and easy use of @msdanalyser, providing all calculations necessary to estimate $< MSD >$ and the ensemble-average α-value (appendix D.2). *a_distribution* was developed to find the distribution of α-values for all trajectories with a goodness of fit $R^2 > 0.8$ from a single timepoint, and creating a histogram of their distribution (appendix D.3)

5 Results

In this section the effects of alginate G-blocks on collagen structure and viscoelastic properties will be presented. Firstly, the structure of collagen networks with variations in concentration, degrees of polymerisation and block-composition of G-block, was investigated by CRM. Secondly, the kinetics of the fibrillation-process was investigated, both by turbidity and TL-CRM. Finally, employing combined MPT and TL-CRM, the changes in microrheology and structures of the developing network was monitored.

5.1 Structure of the Collagen Network

5.1.1 Varying Concentrations of G-block

To investigate the network structure of fibrillar collagen assembled in the presence of G-blocks DPn-12 (actual DP-n = 11.8 as described in Methods 4.1.2), CRM-imaging at gel equilibrium was conducted. The equilibrium gel structures of 2mg/ml collagen gel without added G-block, and with concentrations of 0.05mg/ml and 0.5 mg/mL G-block were imaged after overnight gelling at $40\,^{\circ}$C.
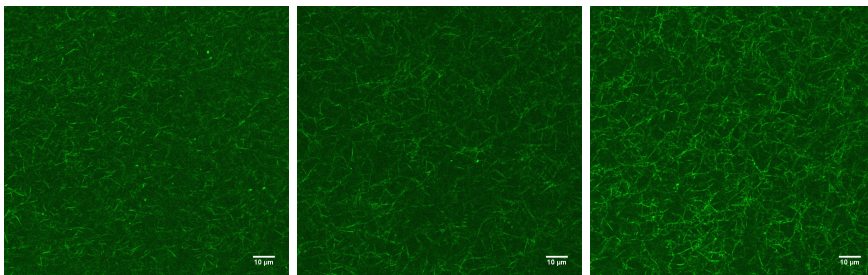
(a) No added G-block   (b) 0.05mg/ml G-block   (c) 0.5mg/ml G-block

Figure 18: Confocal reflectance images of 2mg/ml collagen matrices with varying concentration of G-block DPn-12.

It is clear from figure 18 that the collagen solution forms a remarkably more defined gel upon addition of G-block. The fibres seem thicker, and appear to have aggregated with increasing G-block concentration. The gel in 18c shows a more intertwined and densely connected network with larger fibres compared to the pure collagen gel in 18a. However the pure collagen gel without any added G-block ap-

pears to contain a similar amount of fibres, but the fibres seem thinner and shorter, organised in a less entangled network. The collagen network shown in figure 18b with low concentration G-block (0.05 mg/ml), shows an intermediate network with slightly larger fibres and a somewhat more densely connected network. The effect of G-block is prominent even at low concentrations, considering that the effect of 0.05mg/ml G-block corresponds to a w/w-ratio of only 1:40 G-block/collagen.

To further quantify the effects on the fibre-network, the images were analysed with the MATLAB fibre-analysis functions described in the Methods section (4.2.4. The measurements of the intensity-peaks are given i table 5. This table shows that the pixel-intensity varies independently of G-block addition. There are many reasons why there might be some difference in the pixel-intensity of the pictures, that is not representative of collagen-fibres, but rather of settings or aperture differences. Correcting for pixel-intensity variations by using average-intensity for the cutoff-value, the table shows that number of peaks seems to be decreasing slightly with increased G-block. This indicates that fewer fibres have been formed in the presence of G-block. However, the difference is quite small with only 4 fewer fibres detected in high concentration G-block sample than in the pure sample for a $100\,\mu m$ cross-section.

The average peak-width is largest for the highest concentration of G-block, indicating that the collagen fibres become wider when treated with G-block. However, between collagen samples treated with 0.05mg/ml G-block and no G-block there was no detectable difference in peak-width. The automated fiber-analysis corresponds well with the observed fibre-sizes in images in figure 18.

Table 5: Fibre-analysis of CRM-images from figure 18 with varying concentrations of G-block DPn-12.

	Pixel intensity	Number of peaks	Peak width (μm)
No added G-block	22.18	97.82	0.1323
0.05mg/ml G-block	20.64	77.45	0.1323
0.5mg/ml G-block	23.56	93.54	0.1540

5.1.2   Varying DP of G-blocks

The collagen network structure formed in presence of G-blocks with higher degrees of polymerisation was investigated. The gels were again visualised by CRM-

imaging after overnight gelling at $40\,°C$. The highest G-block concentration of 0.5mg/ml was used for all samples, but the type of G-block now included DPn-24 and DPn-33 in addition to the DPn-12 that showed to alter structure in the previous experiment. Note that DP is the number-average degree of polymerisation, with a composition of multiple different chainlengths.

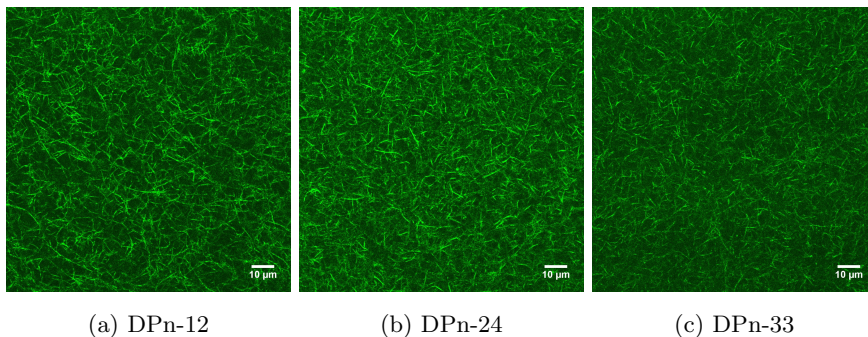(a) DPn-12   (b) DPn-24   (c) DPn-33

Figure 19: Confocal reflectance images of 2mg/ml collagen matrices with varying chain lengths of G-block in a 0.5mg/ml concentration.

As seen in figure 19, the G-block effect on the collagen network structure is more prominent in the shorter chained DPn-12 and DPn-24. Fibrillar network formed in the presence of DPn-33 G-block has an altered structure compared to the untreated collagen gel (fig 18a), but the fibres show only a slight increase in diameter, and the network still seems quite densely connected. The short-chained G-block oligomers seem to evoke a stronger effect on the collagen network-structure. However, the molar concentration of G-block DPn-33 is lower than that of DPn-12, as less molecules are added when weighing out a sample of higher molecular weight. Accounting for 3x lower molar concentration of the $\sim$3x higher M_W sample, the shorter chained G-blocks still seem to have the strongest effect when comparing 0.5mg/ml G-block DPn-33 with the 0.05mg/ml G-block DPn-12 (figure 19a).

Similar results are also observed when running the fibre-analysis on the pixel-intensities from the pictures. As seen in table 6 the pixel-intensity is quite high in DPn-24 gel, which corresponds to the brighter fibres observed in figure 19b. The analysis showed that G-block DPn-24 produces more collagen fibres, and that they were larger in diameter. However, from manual measurements of the images it appears that the fibres in DPn-12 sample are in fact wider. The automatic analysis appears to have issues distinguishing between the structures in the intensely reflecting image. Table 6 show that fibre-number and fibre-diameter appears lower

in DPn-33 which corresponds well with the observations from the image. Since each DP- is a number average degree of polymerisation, and actually contains a mixture of different polymer lengths it is possible that the observed effect in DPn-24 and DPn-33 is in fact the effect of a small fraction of shorter chained oligomer within the DP-average sample. Appendix A.1 shows that there is a large content of low-molecular weight molecules within the DPn-24 and DPn-33 samples. This could explain why figure 19c of DPn-33 appears to have a similar collagen network-structure as the low concentrations of G-block DPn-12 in figure 18b.

Table 6: Fibre-analysis of CRM-images from figure 19 with varying degrees of polymerisation. Accurate DPn is given in table 1.

	Pixel intensity	Number of peaks	Peak width (μm)
DPn-12	26.75	143.27	0.2369
DPn-24	29.63	169.36	0.2615
DPn-33	24.96	157.18	0.1893

5.1.3 Varying Block-Composition

The structure of the collagen network in the presence of alginates with other block-compositions was investigated. In addition to G-block, a gel was prepared containing M-block, both in concentrations of 0.5mg/ml. To keep the chain-lengths as comparable as possible, G-block with DPn-24 and M-block with DPn-20 was chosen for this experiment. The gels were visualised by CRM-imaging after overnight gelling at 40 °C.

From the images in figure 20, it can be observed that the effect of M-block appear to be identical to the effect of G-block chains of similar lengths. There is a noticeably more "defined" collagen network in both alginate-containing gels compared to the reference gel. The fibres look larger, brighter and more intertwined. The structural differences in the fibre-network can also be shown by applying the fibre-analysis.

Table 7 shows again that the collagen gel containing M-block had similar alterations in network-structure as the collagen gel containing G-block. Both pixel-intensity, number of peaks and width of peaks is near identical in the two samples. The collagen fibres seem to increase in number and width upon addition of alginate oligomers, regardless of block-conformation.
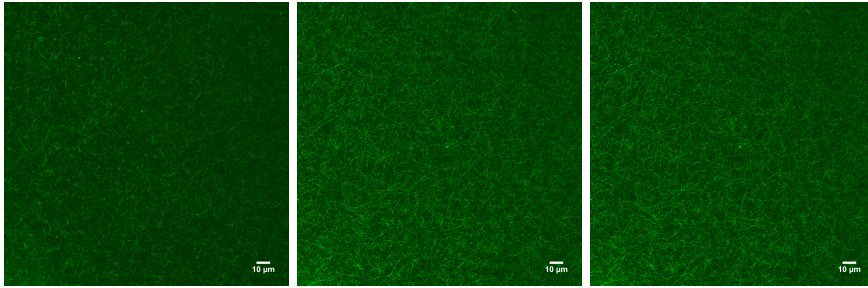
(a) No added alginate   (b) G-block with DPn-24   (c) M-block with DPn-20

Figure 20: Confocal reflectance images of 2mg/ml collagen matrices with varying block composition. 0.05mg/ml of M-block DPn-20 and G-block DPn-24, with pure collagen sample for reference.

Table 7: Fibreanalysis of CRM-images from figure 20. with varying block composition.

|	Pixel intensity	Number of peaks	Peak width (μm)
No added G-block	22.92	140.73	0.1458
G-block DPn-24	28.10	272.27	0.1682
M-block DPn-20	27.93	267.09	0.1696

5.2 Turbidity

The kinetics of collagen fibrillogenesis with varying content of G-block DPn-12 was monitored by turbidity assay as a validation method for the subsequent TL-CRM method. The increase in turbidity of the solution was measured as absorbance at 400nm by a spectrophotometer. Three different gel concentrations made according to table 2 were analysed at room temperature ($25\,^\circ\mathrm{C}$) for turbidity, and at the lowest achievable temperature for TL-CRM ($30\,^\circ\mathrm{C}$).

As seen in figure 21a the turbidity-time curves of collagen fibrillogenesis were sigmoidal. After an initial lag-phase, the turbidity increased exponentially until it reached a plateau level. The turbidity-time curve shows a clear difference in kinetics of the gels depending on G-block content. The sample with high concentration of G-block (0.5mg/ml) had a faster turbidity development compared to the collagen samples without G-block. The low concentration G-block (0.05mg/ml) showed an unexpected development of turbidity, with an extended lag-phase and poor growth. There were some airbubbles present in the sample, which might have

interfered with the result.

Comparing the turbidity-time curve with the graph of pixel-intensity-development measured by TL-CRM, it is clear that the two different methods provide similar results. The intensity of reflected light measured by TL-CRM increases in the same sigmoidal manner as scattering of light by spectroscopy. The difference between sample with and without G-block is apparent by both methods. The low concentration G-block (0.05mg/ml) also showed a deviant pixel-intensity-development. This can be explained by some aggregation or "lump" of fibres observed in regions of the images.
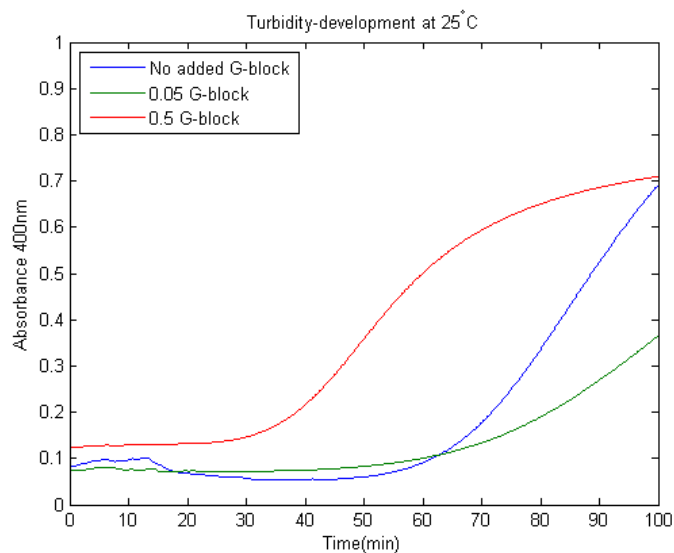
(a) Turbidity by spectrophtometry
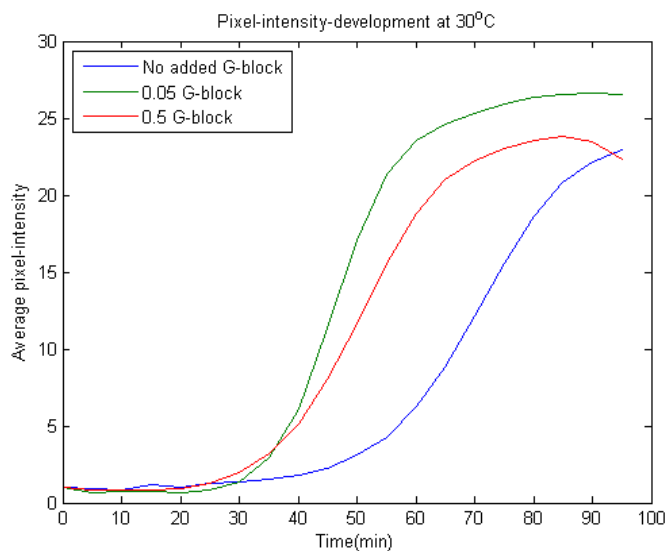
(b) Pixel-intensity by TL-CRM

Figure 21: Kinetics of collagen fibrillation monitored by spectropho-
tometry and TL-CRM. 2mg/ml collagen solution with varying concen-
trations of G-block DPn-12. The incubation-temperatures depended
on method, with spectrophotometry at 25 °C and microscopy at 30 °C.

39

5.3 TL-CRM

The samples with varying concentration of G-block DPn-12 were subjected to temperature-controlled time-lapse study of fibre-development. The temperature on the microscope was kept at 37 °C with a warm air incubator. Reflectance images were taken every 2.5min, for a total of 90min. The microscope settings were identical for all samples, and are presented in their entirety in appendix B.1.

The G-block effect on structure and kinetics is presented as videos in attached zip-files. Figure 22 shows the CRM-images from selected time-points 10min, 20min, 40min and 80 min after initiation of fibrillation. Initially, at 0min and 2,5 min, no structures can be resolved in either gel. The first fibres appear at 10min in the sample with highest G-block concentration (0.5mg/ml). For the 0.05mg/ml G-block sample the first collagen fibres appear after about 20min, and for samples without G-block the fibres appear first after 30min incubation. A "haze" or "halo" of non-fibrous collagen can be observed surrounding the developing fibres in all samples. The small bright particles observed in the images are the fluorescent particles used for MPT described in the next section. The final network structures corresponds well with the network-structures observed from overnight incubation in experiment 1 (figure 18).

The total intensity of the CRM-images at each timepoint was plotted as a function of time presented in figure 23. All plots were corrected for the intensity from time-point 2.5min, which corresponded to noise and reflected light from the microscope. Correcting for this it is clearly shown that increasing concentration of G-block shortens the lag-time for fibrillogenesis. The lag-time before the reflectance starts to markedly increase is longest in collagen without G-block (30min), and almost no lag-time is observed for the sample containing 0.5mg/ml G-block (<10 min). The rate of reflectance-increase after the formation of the first fibers appears to be the same for high and low concentration of G-block. For pure collagen gel however the rate is low until 70min incubation, where it increases to a growth-rate similar to that of samples containing G-block.

The decline in pixel-intensity for 0.5mg/ml G-block at late time-points can be explained by an issue with the microscope. The droplet on the objective lens had a tendency to evaporate at late stages of the time-series. This is due to the elevated temperature, and fan used to distribute the hot air. Evaporation of the water droplet occurred for multiple samples, and showed a similar decrease in intensity of the image as seen in here in 0.5 G-block.
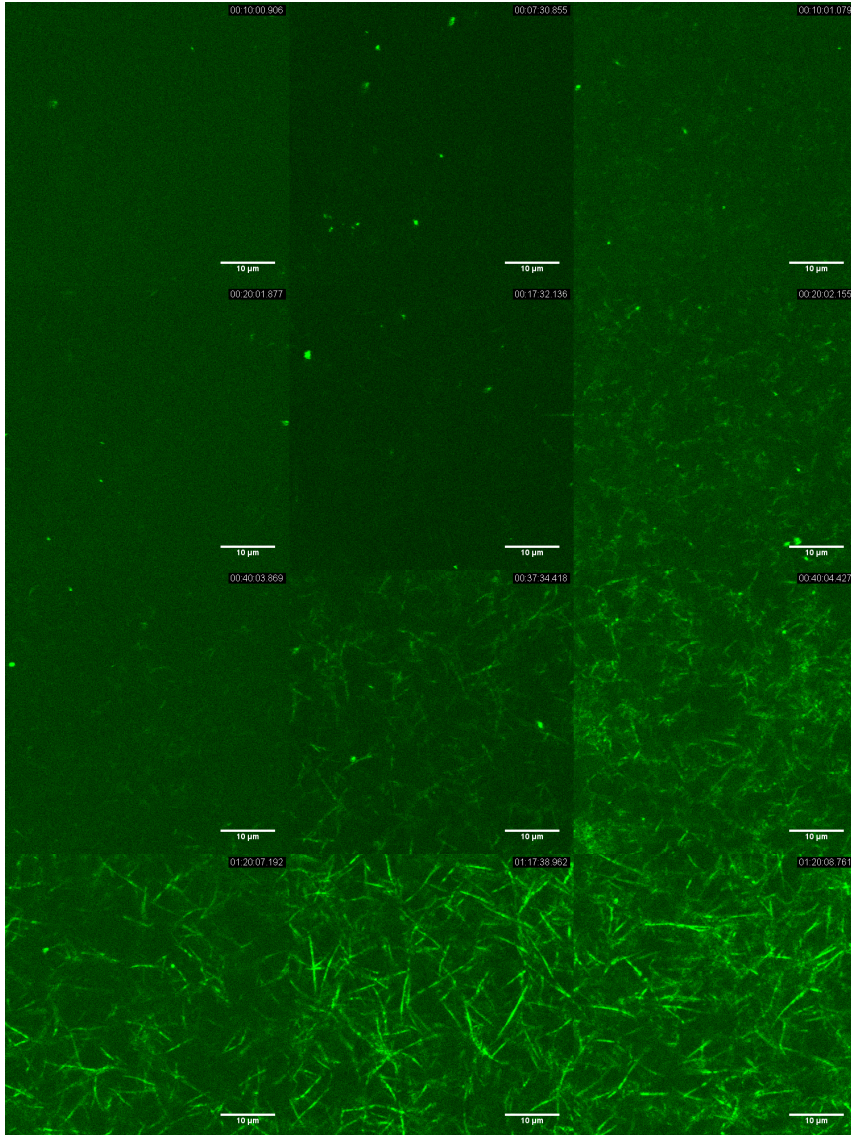
Figure 22: Confocal reflectance images of 2mg/ml collagen fibre-networks formed in the presence of varying concentration of G-blocks. Concentration of G-block is from left to right, no added G-block, 0.05mg/ml G-block, 0.5mg/ml G-block. The timepoints of imaging are from top to bottom 10 min, 20 min, 40 min, 80 min after initating gelation.
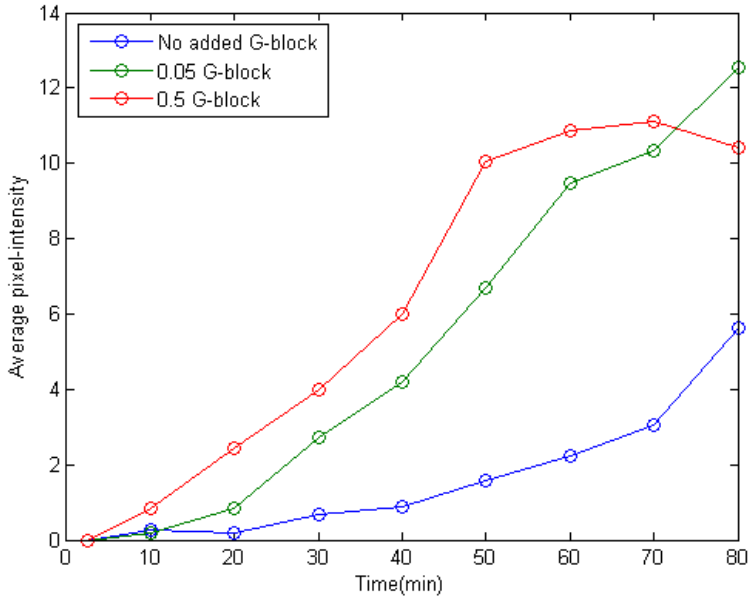
Figure 23: Pixelintensity in CRM-images plotted as a function of time of gelation. Corrected for reflectance in image at t=2.5min. The samples contained 2mg/ml collagen and varying concentration of G-block DPn-12.

From the same time-series, fibre-width and number of fibres were estimated by the fibre-analysis described in the Methods section (4.2.4. The resulting graphs seen in figure 24 shows an increase in both fibre width and fibre-number with higher concentrations of G-block. Number of fibres seem to correspond closely with overall intensity-development. Width-of-peaks is not an accurate representation of actual fibre-width. The curves for width-development over time are a bit "jagged", but seem to indicate an almost linear growth of fibre-diameters with time.
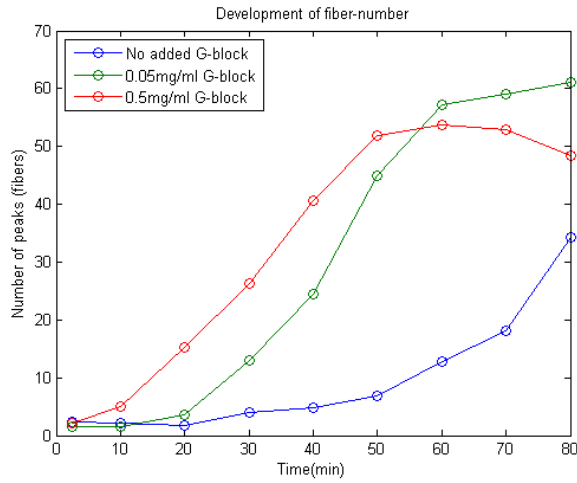
(a) Average number of fibres in a 50 µm crossection of TL-CRM-images of a developing collagen network, plotted as a function of time.
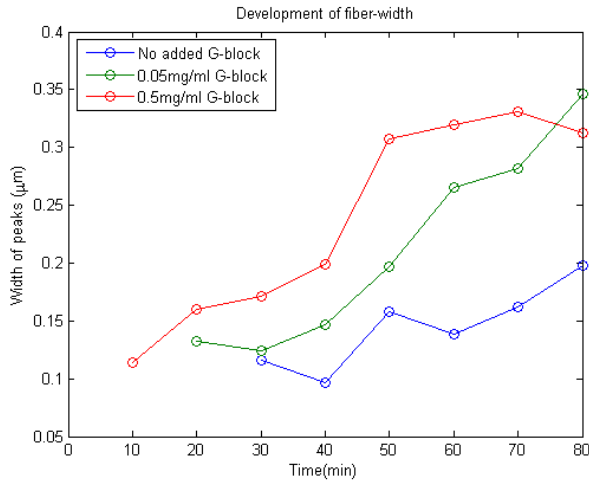
(b) Average diameter of fibres in a 50 µm crossection of TL-CRM-images of a developing collagen network, plotted as a function of time.

Figure 24: Fibre-analysis of the pixel-intensity-profiles along horizontal lines in 50 µm large section. The samples contained 2mg/ml collagen and varying concentration of G-block DPn-12.

5.4 Multiple Particle Tracking

5.4.1 MSD in gels with varying G-block concentration

The fluorescent particles (0.5 µm diameter polystyrene microspheres with carboxylated surface) in the collagen-G-block gels were tracked for a 20s duration every 2.5 min over a 1h 30 min period as described in Methods section 4.2.3. The same collagen gels from TL-CRM with no added G-block, 0.05mg/ml G-block and 0.5mg/ml G-block were investigated. As an example of analysis the time-series from the 30min timepoint will be presented first, representing a time at which all samples have developed some fibres, but there is a marked difference in the collagen network-structure of samples treated with different G-block concentrations.

(a) no added G-block   (b) 0.05mg/ml G-block   (c) 0.5mg/ml G-block
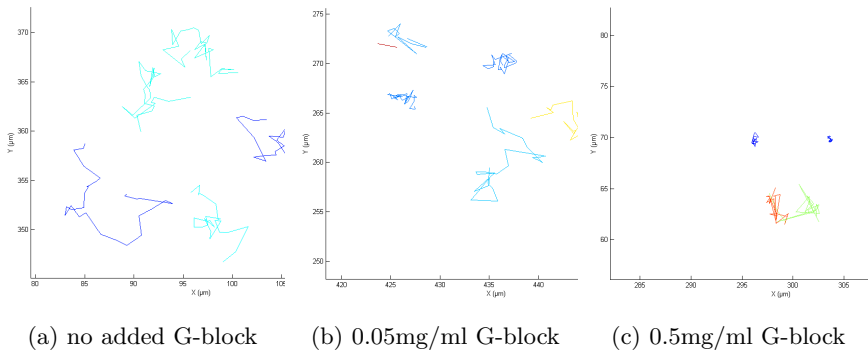
Figure 25: Plotted trajectories of particles (0.5 µm diameter polystyrene microspheres with carboxylated surface) after 30min of gelation. All samples contained 2mg/ml collagen, but vary in concentrations of G-block DPn-12.

Simply by plotting the xy-coordinates of the trajectories, a difference in particle mobility in the collagen gels can be observed after 30 min of gelation. In the collagen-network formed without the presence of G-block the particles appear to move freely with an unrestricted motion as seen in figure 25a. In the collagen-networks formed with G-blocks present the particles appear to move less freely, with trajectories restricted to a smaller area as seen in figure 25b and 25c.

The MSD as a function of time for each trajectory is calculated with @msdanalyzer using equation 8. The MSD of ∼100 trajectories are plotted in the upmost graphs in figure 26. As observed from the plot, some trajectories seem to be erroneously linked in the particleTrackerJ-program, resulting in some odd lines. The

ensemble-mean MSD ($< MSD >$) is calculated with @msdanalyzer by equation 10. This takes the average over all the curves, making the few erroneous trajectories a negligible noise. The bottom plots in figure 26 shows that $< MSD >$ has the steepest slope for collagen gel without G-block, and gentler slopes for gels containing higher G-block concentration. The first 25% of $< MSD >$ is used to estimate the ensemble-average diffusion coefficient illustrates with the red line in figure 26. Through linear weighted fit of the mean MSD curve the diffusion coefficients were calculated; with no G-block D = 1.97±0.10, with 0.05 G-block D = 1.03±0.05, with 0.5 G-block D = 0.54±0.03, showing a significant difference in particle mobility.

(a) no added G-block   (b) 0.05mg/ml G-block   (c) 0.5mg/ml G-block
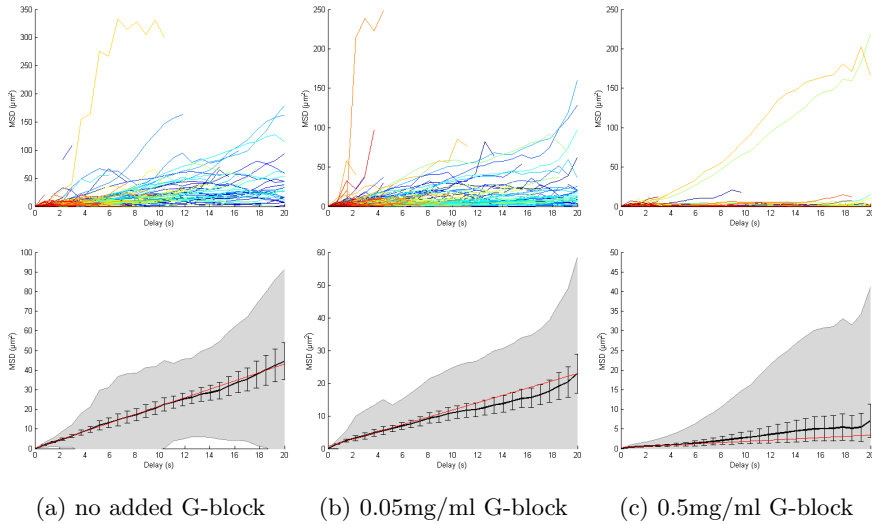
Figure 26: MSD analysis of particle trajectories ($0.5\,\mu$m diameter polystyrene microspheres with carboxylated surface) after 30 min gelation of a 2mg/ml collagen solution with varying concentrations of G-block DPn-12. Above: individual time-average MSD for each trajectory. Below: ensemble average MSD (black line) with greyed area representing the weighted standard deviation over all MSD curves. Red line shows the linear regression from first 25% of $< MSD >$ used to calculate the diffusion coefficient.

5.4.2 MSD-development in Sol-Gel Transition

To monitor the development of vicoelastic properties in the gel, the motion-type of the particles is analysed by log-log-fitting of MSD (eq. 11) obtaining the anomalous exponent (eq. 12). In the following figures the logarithmic MSD-plots and α-value distribution at time-points before, during and after gelation is displayed. The selected times were 2.5min, 30min, and 80 min respectively. Figure 27 shows results from MSD analysis of particles in collagen gel with no added G-block. Figure 28 shows MSD analysis of particles in collagen gel with 0.05mg/ml G-block. Figure 29 shows MSD analysis of particles in collagen gel with 0.5mg/ml G-block.

At 2.5 minutes all of the samples show superdiffusive motion of the suspended particles. In the CRM-images from these early time-points extensive drift can be observed in the samples. This is why the first measurement presented here is after 2.5 min, and not at 0 min, but still the drift seems to largely influence the measurement.

After 30min however, the drift in samples can be considered negligible, as the same fibre-structures can be observed in CRM-images at 27.5min and 30min. At the 30min timepoint the pure collagen gel has a reduced MSD of particle trajectories, with an average α-value of 1, indicating diffusive transport. The collagen samples containing 0.05mg/ml G-block and 0.5mg/ml G-block show an even more confined particle motion, with subdiffusive transport and average α-values of 0.90 and 0.56 respectively at this time in gelation.

After 80min, when the collagen networks seem to have stabilised into their final structure, the dispersed particles in the collagen samples containing G-blocks show strong confinement, with α-values of 0.32 and 0.27 respectively. The MSD in pure collagen gel after 80 min is on average superdiffusive, with MSD-plots and α-value distributions indicating that there is some drift in the sample that might be responsible for this. This observation is supported by the TL-CRM images.

Figure 27: MSD analysis of trajectories of fluorescent particles (0.5 μm diameter polystyrene microspheres with carboxylated surface) in collagen sample without G-block. Measured at times 2.5 min, 30min and 80 min. Graphs showing the MSD as a function of timescale, and the distribution of α-values.

Figure 28: MSD analysis of trajectories of fluorescent particles (0.5 μm diameter polystyrene microspheres with carboxylated surface) in collagen sample with 0.05mg/ml G-block DPn-12. Measured at times 2.5 min, 30min and 80 min. Graphs showing the MSD as a function of timescale, and the distribution of α-values.
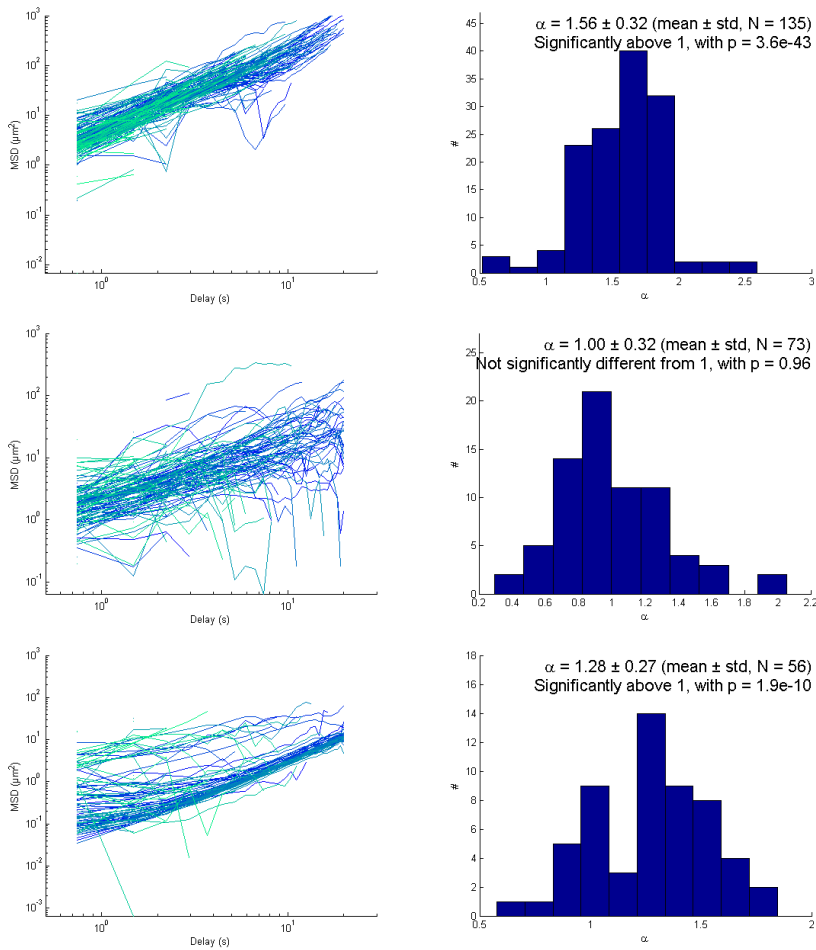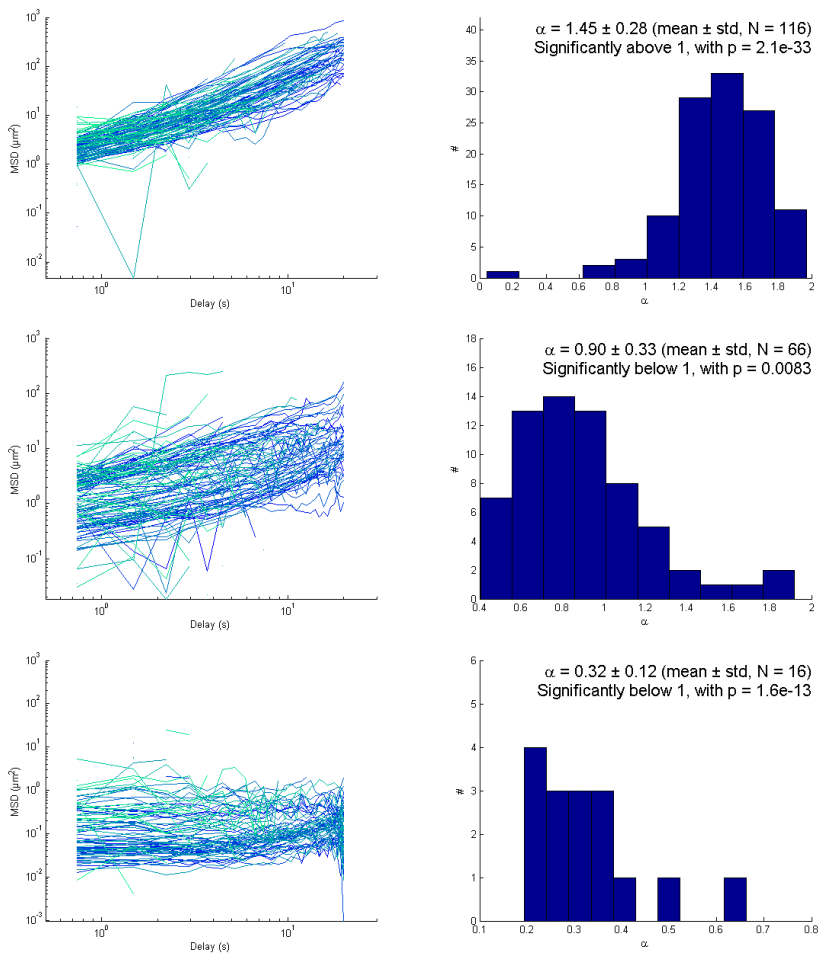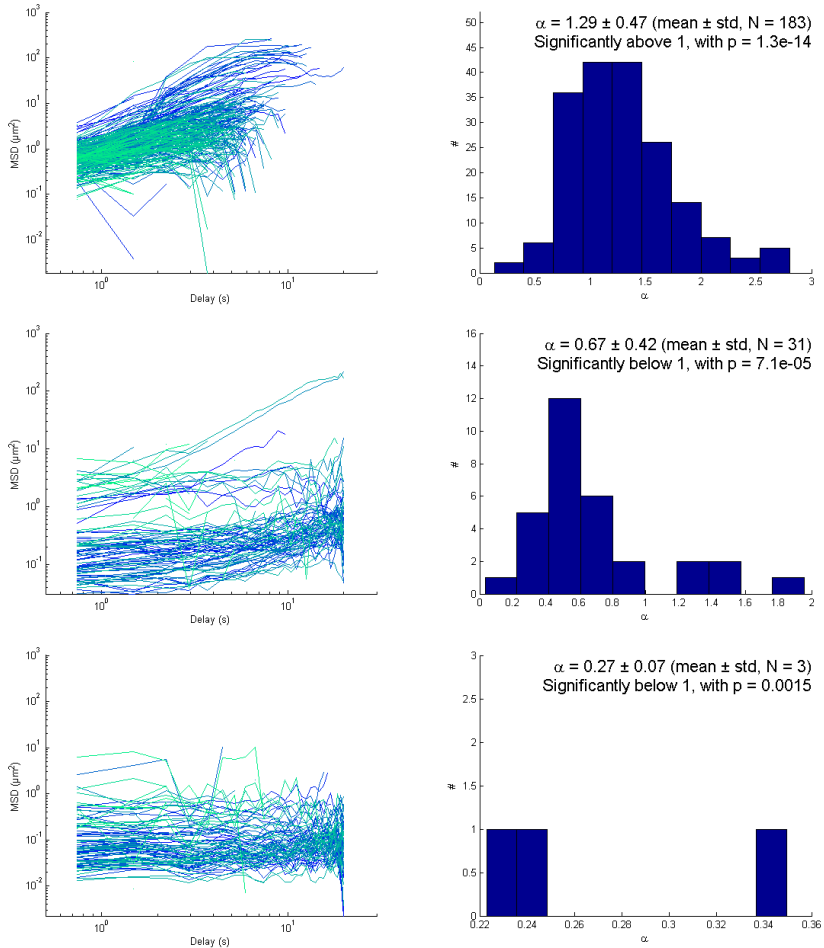
Figure 29: MSD analysis of trajectories of fluorescent particles (0.5 µm diameter polystyrene microspheres with carboxylated surface) in collagen sample with 0.5mg/ml G-block DPn-12. Measured at times 2.5 min, 30min and 80 min. Graphs showing the MSD as a function of timescale, and the distribution of α-values.

Plotting the average anomalous exponent as a function of time, the progression of confinement of particles in the developing gels can be monitored. In figure 30, the development in particle motion in the collagen networks containing different concentrations of G-block is displayed.

Comparing the curves, there is a marked difference in the development of particle motion between the samples with and without G-blocks. The collagen sample without G-block addition has a decrease in motion of the suspended particles, but ends up with an only slightly sub-diffusive motion-type (α=0.77 after 80min). As discussed previously regarding figure 25a, the sample did show some drift in the CRM-images which can partially explain this, but it does also suggest that the network-structure formed without G-blocks present is less of a hindrance for the particles. The collagen samples treated with 0.05mg/ml and 0.5 mg/ml G-blocks both end up with a complete confinement of the suspended particles ($\alpha \approx 0$). There seems to be an equal rate of increasing confinement of the particles, with the major difference between the two samples being the lag-time before confinement begins.
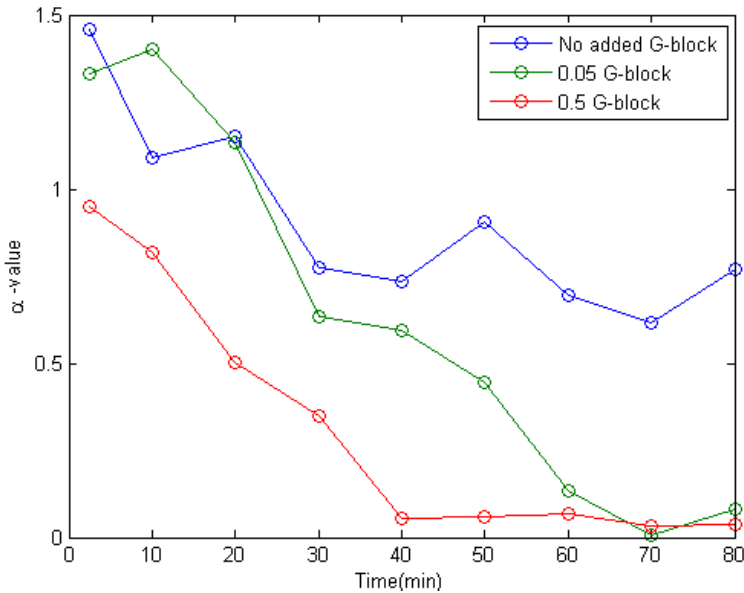
Figure 30: Average anomalous exponent from MSD plots of particle trajectories, plotted as a function of time. Superdiffusive motion ($\alpha >$1) is possibly resulting from drift in the samples. Subdiffusive particle-motion ($\alpha <$1) indicates confinement of particles by the surrounding collagen networks.

5.5 TL-CRM and MPT of 8mg/ml G-block DPn-12

Unpublished studies on G-block effect on *in vitro* cancer-cell cultures have operated with an even higher G-block concentration than presented so far in this thesis. To investigate the effect this might have on collagen fibrillation, the TL-CRM and MPT study was performed with 8mg/ml G-block DPn-12. Note that this is 4x the w/w concentration of collagen (2mg/ml). The full time-lapse videos are given in attached zip-files, selected time-points from TL-CRM are shown below.

(a) 2.5 min   (b) 10 min   (c) 20 min

(d) 40 min   (e) 80 min
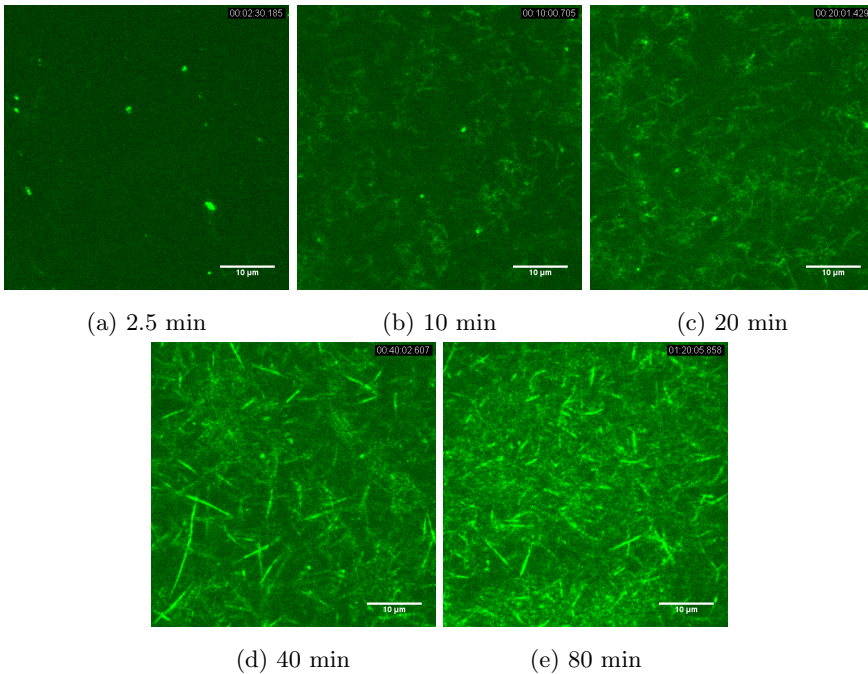
Figure 31: CRM images of 2mg/ml collagen networks formed in the presence of 8mg/ml G-block DPn-12. Selected time-points from the 1h30min gelation period.

From figure 31 it is evident that the high G-block concentration causes a premature fibrillogenesis, with the first fibres forming already 2.5 min after initiation. Although reflective structures are quickly assembled, few take shape of "defined" fibres, but appear to mostly form a dispersed "haze" of reflecting fibre-fragments. The few fibres that are formed are thicker and shorter than native fibres, however the network is to undefined to successfully run the fibre-analysis functions.

Comparing the development of reflection in CRM-images of this high G-block sample to samples with lower G-block-concentrations shows that 8mg/ml G-block causes collagen to assemble more rapidly and overall causes greater light-scattering (fig 32a). After 80 min the collagen sample treated with 8mg/ml G-block reflect light with an intensity almost 3 times that of untreated collagen.

Figure 32b shows the development of ensemble-average α-values of particle trajectories, the measure of confinement of particle motion. 8mg/ml G-block appears to make particle motion subdiffusive already after 2.5 min, the first time-point measured. During gelation there is no notable decline in particle motion as observed in the other samples, but α-values remain at an apporximately constant level throughout the gelation process. Already after 50min the particles have a more confined motion in 0.5mg/ml G-block and 0.05mg/ml G-block samples than in the 8mg/ml G-block sample.

(a) Pixelintesities from TL-CRM (b) α-values from MPT and MSD
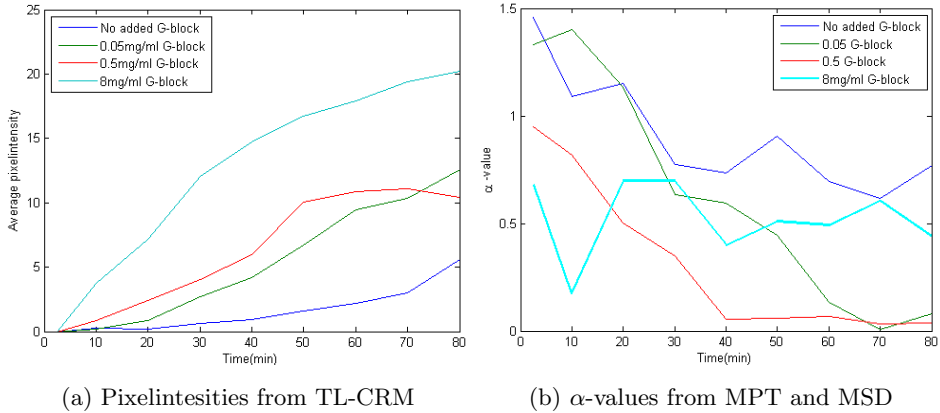
Figure 32: Structure- and microrheology measurements of 2mg/ml collagen samples treated with 8mg/ml G-block DPn-12. Fibre-development is measured by pixel-intensities from TL-CRM and MSD-analysis of 0.5 µm diameter polystyrene microspheres with carboxylated surface tracked by MPT.

6 Discussion

6.1 Nature of the interaction

The self-assembly of collagen monomers into collagen fibrils is a highly sensitive process, influenced by multiple factors. Properties such as temperature, pH and ionic strength has shown to be particularly influential on the stability of the tropocollagen monomers and rate of fibrillogenesis [8, 13]. The temperature is kept constant for all experiments, and the addition of neutralised G-blocks (pKa $\sim$3.5) will not influence the DPBS buffer capacity at pH $\sim$7. The ionic strength contribution from addition of G-block can also be said to be negligible compared to the buffer concentration and other ionic species present in the sample. The ionic strength of the samples are approximately 150mM without G-blocks, while Li [13] reported ionic strengths of 250mM necessary to reduce the degree of collagen gelation under similar conditions. For a G-block concentration of 0.5mg/ml the addition of analyte corresponds to an increase in ionic strength of only 1.3mM, and even the concentration of 8mg/ml G-block corresponds to only 18.5mM increase in ionic strength. From this it can be determined that the observed changes in collagen structure should not be attributed to an ionic strength effect, nor the pH-influence of the G-block. This indicates that there is a direct- or indirect interaction between the G-block and collagen that is the cause for the observed effect on network structure and mechanical properties, yet the nature of this interaction remains to be determined.

In vivo collagen interacts with many different types of molecules. They can generally be grouped into cell-surface molecules, ECM-molecules and growth- and differentiation factors. These interactions have demonstrated to be one of the reasons for the diversity of collagen-network structures observed in different tissues *in vivo* [56]. Of the 50 molecules that have been found to interact with collagen, half of them have specific binding-sites on the protein [56]. Among the molecules with binding sites on collagen, some are structurally and chemically similar to G-blocks such as heparin and it is possible that they interact by the same mechanisms. A particularly interesting comparison for this study is the glycosaminoglycans (GAGs) of the ECM which are partially composed of anionic polysaccharides, structurally and chemically similar to G-blocks as illustrated in figure 33. Multiple studies have been done on the effects of GAGs on type 1 collagen network morphology and strength, but the data are in many cases conflicting due to variations in experimental parameters. Despite the conflicting studies, there appears to be

clear evidence for electrostatic interactions between many anionic polysaccharides and collagen *in vitro* at physiological conditions with seemingly similar effects as observed for G-blocks in this study. A summary of studies on effects of GAGs and other structurally similar polysaccharides is given in table 8. Note that most of these studies have been performed on large polymers of higher Mw than the relatively short G-block oligomers investigated in this study.
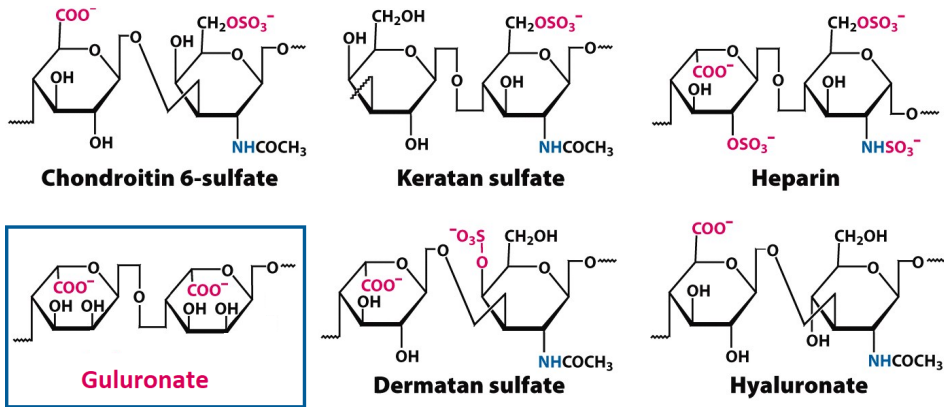
Figure 33: Illustration of the repeating disaccharide unit of some glycosaminoglycans and of a homopolymeric guluronate. Adapted from [57]

6.1.1 Charge

On each of the α-chains in the collagen triple helix there are about 270 positively charged residues, which often appear in clusters along the protein [68]. The high proportion of ionisable residues proposes in itself that electrostatic interactions are important for the stability of the triple helix, and the self-assembly process of fibrillogenesis. The carboxyl-groups of G-block (pKa $\sim$3.5) are ionised at neutral pH, so there is theoretically attraction between the negatively charged G-block to positive charge-clusters on the collage. Neutral pH is close to the isoelectric point of collagen (pI$\approx$7.5 at similar conditions [13]), where it reaches a maximum ionisation of the charged residues. The ionic species that are present will screen some of the charges on both G-block and collagen. Nonetheless, ionic polysaccharides have shown to affect collagen assembly under similar conditions in studies on GAGs summarised in table 8.

Table 8: A summary of the effects of different polysaccharides on type I collagen. The effect on collagen kinetics of fibrillation, fibril-diameters, and mechanical properties of the resulting gel was compared for multiple studies. The grading system signifies an observed effect (+) or no effect observed (-) on the respective properties, multiple symbols means the same results have been observed in multiple studies. Inspired by [58].

Name	Abbr.	Charge	Kinetics	Size	Strength	Sources
Hyaluronan	Hyal	Anionic	++	++	++	[59–61]
Heparin	Hep	Anionic	++	+++	+	[37, 60, 62–64]
Heparan S	HS	Anionic	+	+	+	[60]
Chondroitin S	CS	Anionic	++	++	+-	[58, 60, 62, 65]
Dermatan S	DS	Anionic	+	+	+	[60]
Keratan S	KS	Anionic	-	-	-	[60]
Dextran	Dex	Uncharged	+	-	-	[58, 66]
Chitosan	Chit	Cationic	+	+		[59]
Alginate	Alg	Anionic	+-+	++		[59, 66, 67]

The density of charges on the polysaccharides has shown to be of importance in these studies, and the interactions were abolished at an increased ionic strength, indicating that the interactions were in fact electrostatic in nature. Comparison has also been done for cationic polysaccharides, where chitosan which has a positive charge at neutral pH (pKa~6.5) has shown to increase the fibre-diameter of collagen, but with only minor influence on kinetics according to Tsai et al. [59]. Tsai et al. also concluded that the interaction between chitosan and collagen is electrostatic in nature. For comparison, uncharged polysaccharides such as dextran, agarose and starch did not demonstrate any influence on collagen structure or fibrillation-kinetics [66].

Of particular interest is the apparent importance of uronic acids in the polysaccharides affecting collagen. In a study by Obrink [60] comparing effects of different polysaccharides on collagen, keratan sulphate was the only polyanion not altering collagen fibrillation in any form. KS is structurally and chemically similar to the other GAGs in the experiment, but it contains a galactose sugar instead of a uronic acid sugar (see figure 33). Studies by Tian et al. [69] on the interactions of CS and collagen, suggests that the charged sulphate or carboxyl-groups interacts with the ε-amino group of lysine or the guanidine group of arginine via electrostatic

interaction. KS does contain negatively charged sulphate-groups, but still did not alter collagen fibrillogenesis in the studies by Obrink [60]. They proposed this to be a result of the lower charge-density of the polymer, or that the missing uronic acid is essential for the collagen-interaction.

Obrink [60] also observed differences in collagen complex formation with CS notably containing D-glucuronate as the only hexuronic acid, and DS containing mixes of the steroisomers D-glucuronate and L-iduronate. Similar to the alginate monomers, these hexuronic acids are also C5-epimers. They adopt different ring-conformations, with α-L-iduronate in a $_1C^4$-conformation bearing the closest resemblance to the α-L-guluronic acid of G-blocks. The linking chemistry is different however, with CS and DS being β1-3 linked, and alginates having α1-4 glycosidic linkages. In the study by Obrink, DS had a larger impact on collagen fibrillogenesis than CS, indicating that L-iduronate has a stronger effect than D-glucuronate on the collagen monomers. No notable differences in collagen structure was observed from treatment with G-block or M-block in this study as seen from figure 20. However, more in depth studies should be performed to properly asses the importance of the sterochemistry of alginate-monomers in the interactions with collagen.

Few studies have previously been performed on the interactions of alginates and collagen, as its potential as a therapeutic has not been extensively explored. Some studies have been done on alginates and collagen as components of composite scaffolds for tissue-regeneration purposes. A study by Sang et al. [67] on this reported an altered network-structure of large twisted collagen fibrils, similar to what has been observed in the present study. Sang et al. suggested that the alterations arised from electrostatic complexation between the alginate polymers and collagen. Elution experiments from their study showed capturing of alginate within the collagen-fibre network, further supporting that electrostatic interaction had occurred.

6.1.2   Size

DPn-33 chains are nearly 3x as long as DPn-12 chains, and are consequently in 3x lower molar concentration in the sample when measured by weight. The inferior effect on collagen structure by DPn-33 observed in figure 19c can in part be attributed to the lower number of interacting G-block molecules. However, there is still a larger structure-modification by low concentration DPn-12 (0.05mg/ml),

than observed in DPn-33 (0.5mg/ml), indicating that this is not exclusively the result of molar concentrations, but is also related to the chain-lengths of the alginate.

One hypothesis explaining the interaction between collagen and alginate is cooperative binding, where the G-block can act as a linker, facilitating the association of different collagen molecules. This has shown to be the case in studies of the anionic polysaccharide heparin. Heparin has been suggested to work as a cross-linking molecule, with specific binding-sites on collagen forming "heparin-bridges" between the tropocollagen building-blocks, facilitating their assembly. San Antonio et al. [70] employed electron microscopy to visualise the site of heparin interaction near the amino-terminus of the type I collagen monomers. They found a heparin binding site, with highly basic triple helical domain consisting of amino-acids known to associate with disaccharide epitopes. In the process of lateral aggregation, the heparin-molecules become entrapped, and end up intercalated within the collagen fibres [64]. It is assumed that longer chained molecules will have the strongest effect on cooperative binding, since they can facilitate interaction with more charged clusters along the collagen-molecule, and the strength of the interaction would be higher.

In this study however, the shorter chain-length of G-block (DPn-12) gave a more pronounced effect on collagen structure than longer G-block chains with DPn-24 or DPn-33 as seen from figure 19. A study by Xin et al. [61] describes a similar responses on collagen scaffolds by treating with varying sizes hyaluronan. They saw enhanced vicoelastical properites of collagen gels treated with low Mw HA($M_W = 1.55 \times 10^5$g/mol). High Mw HA ($M_W = 1.2 \times 10^6$g/mol) did not induce similar mechanical improvements. This result was unexpected, as the high Mw HA possesses stronger viscoelastic properties. The researchers concluded that the larger HA molecules formed homologous interactions and entanglements, reducing their and collagens mobility in solution, as well as creating topological hindrance of interactions. The study by [61] used higher concentrations of HA (10mg/ml) than in the present experiment, and both of the weight compositions compared are far higher than what is used in this thesis with an estimated $M_W = 2.16 \times 10^3$g/mol for DPn-12.

As both DPn-24 and DPn-33 guluronates still have rod-like conformations, entanglement and resulting reduced mobility is not a satisfactory explanation for the reduced effect of the longer-chained G-block on collagen monomers. Still, the longer rods can produce some topological hindrance of interactions compared to

DPn-12. The rotational relaxation time (the tumbling of a molecular entity in a viscous medium) becomes larger depending on the molecular weight and concentration of the rod-like macromolecules [27]. If there is a specific structural eptiope on the G-blocks that has to be available for interaction with the tropocollagen, the longer G-block chains will have a reduced interaction-potential resulting from the larger rotational relaxation time.

6.1.3 Mode of interaction

The kinetics of collagen fibrillogenesis has shown to be considerably altered by the addition of G-blocks in this study. The self-assembly of monomeric tropocollagen into a fiber-network was measured by the increased scattering of light, resulting from growth in number of fibres and the increase in fibre-sizes. This was monitored both as turbidity measured by spectrophotometry and as intensity of reflected light by TL-CRM. Both methods detected a remarkable shortening of the lag-phase of fibrillation upon treatment with increasing concentrations of G-block. This has been demonstrated by turbidity at 25 °C in figure 21a, and by TL-CRM at 30 °C in figure 21b and at 37 °C in figure 23.

The lag-phase or "nucleation phase" is the first step in fibrillogenesis, where the first few tropocollagen molecules have associated to form nucleation-centres from which the further aggregation proceeds. Interestingly, the rate of growth of the nuclei into larger fibres seems to be equally as steep with and without G-blocks. Although the intensity development in pure collagen network is slow at first, the maximum rate seems equivalent to that of high concentration G-block (see figure 23). The influence of guluronate oligomers primarily on the lag-time of fibrillogenesis kinetics, suggests that the two-step mechanism of collagen assembly is not affected as a whole, but acts solely on the formation of nucleation centres.

These results contradicts the findings of Sang et al. [67] who saw an *increased* lag-time of collagen fibrillogenesis upon increasing alginate concentrations. The study of Sang et al. was done under similar conditions and concentrations, but with alginates of higher molecular weights (not listed, but 2400cps for a 2wt% solution at 25 °C). However, they also observed an effect primarily on the nucleation-phase, while the rate of fibrillogenesis was otherwise unaffected. Studies on other charged polysaccharides also show the kinetics of collgaen fibrillogenesis to be the primarily affected at the nucleation-stage [37, 60–63, 67].

The G-block effect on the nucleation of fibres is supported by studying details of the

CRM-images. In figure 22 there are visible "halos" of fibre-fragments surrounding the large fibres, which are increasingly present in samples with higher G-block-concentrations. This is even more prevalent in the sample of 8mg/ml G-block as seen in figure 31. In this figure there is an abundance of fibre-fragments, and few complete fibres formed compared to the other collagen samples. The incomplete fibre-formation observed in the 8mg/ml G-block DPn-12 sample can be explained by the high ratio of G-block to collagen (4:1 w/w-ratio). The G-block-collagen interaction caused an elevated formation of smaller aggregates (nuclei), but the lateral aggregation and growth of the nuclei was hindered by the high presence of G-blocks reducing their association and inhibiting the complete assembly of fibres.

The width of the collagen fibres are also affected by G-block addition as observed in the CRM-images and displayed in graph 24b. Wood [62] found that the width of the collagen fibres is determined by the nucleation and shape of the nuclei. His findings suggested that the collagen precipitates onto the early formed nuclei similarly to how crystals grow. Thus the majority of precipitation will occur by growth of those nuclei formed early in the reaction, and they will reach the largest diameters. This corresponds well with what is observed in this G-block experiments, where the diameters of fibres grow with similar rates irregardless of G-block concentration, but the high-concentration G-blocks makes collagen form fibres at an earlier timepoint, resulting in larger fibre-diameters at the end of fibrillation.

6.2   *In vitro/In vivo* disagreement

The aim of this thesis was to investigate the effect of G-blocks on collagen-fibrillation in an isolated system, to elucidate if this is responsible for the observed effects of Rixova *in vivo*. In mouse models of solid tumours, the abnormally dense collagen network in the tumour micro-environment (TME) appears to become more sparse with Rixova treatment. This "normalisation" of TME, or even a "patchy" and incomplete collagen network is postulated to be the reason behind the promising anti-tumour effect of the drug-candidate. However, the effects seen from G-block on type 1 collagen in this *in vitro* study is quite the opposite. G-blocks have in this study yielded thicker collagen fibres in a more dense and interconnected network with increased mechanical strength.

Although parameters such as temperature, ionic strength, pH and dosis are set to replicate conditions *in vivo* (the max concentration of G-block given *in vivo* is

0.25mg/ml), a lot of factors are still different in this simplified *in vitro* system. Since the aim of this study was to investigate the effect on collagen specifically, it is an isolated system with no other components that are naturally present in the ECM. Obviously any interactions between G-block and collagen *in vivo* is likely to be not only an interaction between these two molecules, but might include other componenets which can drastically alter the outcome of the interaction. As described initially the "self-assembly" of collagen is guided and directed by a multitude of molecules *in vivo* and it is possible that the G-block effect *in vivo* is the result of interactions with any of these components rather than with the collagen itself [10].

Another important difference between *in vitro* and *in vivo* studies of collagen fibrillogenesis is that the G-block is present during the whole assembly process. Assembly, disassembly and reassembly is a dynamic process *in vivo*, where G-block will be present during all phases. In the *in vitro* study it is exclusively the assembly of collagen network that is observed. In studies of other GAGs the effect on rate of fibrillogenesis is dependent on whether the GAG is introduced before or after the nucleation phase. However, the nucleation-phase is different *in vivo* where collagen can nucleate on already-present fibril fragments. Since the main effect in this study was seen on the nucleation-stage of fibrillogenesis, it is likely that the effect of G-blocks on remodelling existing network structures *in vivo* would not be as prominent.

From a safety perspective, it is a good thing that G-blocks did not appear to inhibit the assembly of collagen fibres. This would be a mechanism of action that gives a poor safety profile for the drug candidate, considering the essential role of collagen-fibres in tissues. The effect of G-blocks seen in this experiments, where it merely modulates the collagen fibre-assembly, will probably have a better safety-profile and greater potential for for development of the candidate drug into a viable therapeutic.

6.3   Combining TL-CRM and MPT

This study has provided insight into the effect of G-blocks on the collagen-network formation and gelation process. To observe the change in structure and viscoelastic properties, a new method for monitoring gelation has been developed. TL-CRM has been extensively used the last years for visualising network formations [37], and MPT is proven a good method for monitoring microrheological properties

during gelation [45], however the simultaneous use of these two methods is a new and unique tool for monitoring the sol-gel transition. The concurrent study of structure and mechanical properties in a developing gel network has provided new insight into the relationship between the structure and strength formed in a gel. Observing the graph of intensity-development in TL-CRM and α-values from MSD by MPT in figure 34 the correlation between fibre-development and decrease in mobility of the suspended particles is obvious.

(a) Pixel-intensity by TL-CRM

(b) α-values by MPT and MSD
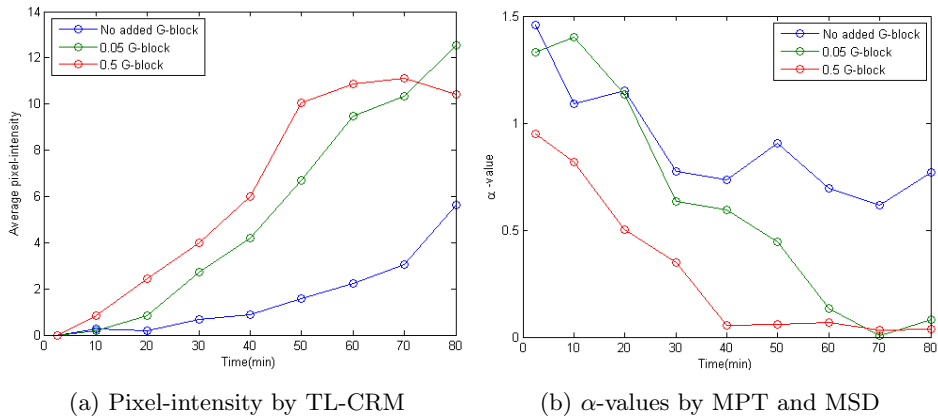
Figure 34: Comparing structure and microrheological measurements of 2mg/ml collagen samples treated with varying concentrations of G-block DPn-12. Fibrillogenesis is measured by pixel-intensities from TL-CRM, and MSD-analysis of 0.5 µm diamtre polystyrene microspheres with carboxylated surface tracked by MPT.

The first visible fibres appear after 10 min in 0.5mg/ml G-block, after 20 min in 0.05mg/ml G-block and after 30min in collagen sample with no added G-block. Looking at the MSD-plots, these first fibre appearances corresponds to the first time the particles show a subdiffusive motion with α-values less than one. This gives a clear evidence for the intuitive notion that fibre-development goes together with a reduction in motility within the network. Although the method is promising, each of the two techniques it combines comes with their own limitations that will be described more in detail below.

61

6.3.1 TL-CRM

TL-CRM is as stated previously a non-invasive method of optical slicing and imaging of the reflecting collagen fibres. The theoretical resolution of confocal reflectance microscopy is 200nm, while the smallest collagen fibrils can have a diameter of only 30nm [10]. This means that early structures formed in the fibrillogenesis process cannot be detected. Since the influence of G-block is suggested to be in the early nucleation stage, it is unfortunate that the structures of this phase are partly invisible by TL-CRM. However, other microscopy options with improved resolution such as electron microscopy methods (SEM or TEM) comes with other limitations that would make it incompatible with simultaneous MPT.

The fibre-analysis functions developed for measurements of fibre-diameter and fibre-numbers are quite simple and unrefined. The horizontal lines selected will not give a perfect cross-section of fibres for the calculation of diameters, as some fibres may lie along the selected line and give an apparently large fibril-diameter. The reflecting "halo" of microfibrils surrounding the fibres is also an issue for detection of individual intensity-peaks. In addition reflectance microscopy has the issue of diffraction artefacts from light from the fibril edges making the fibres appear larger than they are, resulting in an overestimation of intensity-peaks. Although not a perfect method for investigating single fibres and exact quantitative measurements, it does give a good indication of qualitative bulk differences between the different gel compositions. As seen in figure 24 the analysis does nicely display the differences in fibre-number and diameters as a function of time that can be observed from the TL-CRM-images.

6.3.2 MPT

The development of viscoelastic properties of the samples during gelation was investigated with MPT and MSD-analysis. Fluorescent particles were added to the sample prior to initiating gelation, and their motion was captured throughout the sol-gel transition. The main problems arising with the technique in this experiments was drift in the sample, and some aggregation of particles in high-concentration regions of collagen. The movement of particles should not disturb the process of fibrillogenesis, as the driving forces are to small to lead to deformation of microstructure. In this experiment, MPT was only preformed in two dimensions, not tracking particles travelling in z-direction. This means particles with high mobility could just be tracked for shorter periods of time as seen for

example in figure 27. Additionally MSD-analysis occasionally has an issue with wrongly connected trajectories in the software, giving rise to some of the strange trajectories seen in the MSD-plots.

As described in the Technical Introduction, microrheology can in contrast to macrorheology show the heterogeneity of the gel system. Observing the MSD-plot and α-value distribution during gelation (at 30 min in figure 29), the heterogeneity in particle motion is discernible. Some particles still show diffusive motion since they are suspended in the low viscosity fluid within the pores of the collagen network, while others display a highly confined motion showing association to the elastic fibres. The $< MSD >$ used to estimate the anomalous exponent characterising particle motion, is the ensemble-average of all the particles from that timepoint. This means the heterogeneity of the solution is no longer detectable when plotting α-values as a function of time, as $< MSD >$ cannot distinguish between viscoelastic properties of the network element or microrheology of the fluid within the network. However, the bulk rheological properties measured by the averaged α-values has shown to be a good tool for comparison of gelation kinetics when adding varying concentrations of G-blocks to the collagen samples. The ensemble-average confinement of particles, irregardless of where they are located, will still give a representation of mean particle mobility gelation.

The nanoparticles used for MPT were carboxylated, and have a negative surface-charge at neutral pH. It is therefore likely that they interact to some extent with the positive charges on the collagen-network. If the aim is to solely monitor the viscosity within the pores of the network, the particle interaction with the collagen-matrix can be minimised by PEGylation of the fluorescent spheres. By covalently attaching polyethylene-glycol (PEG) to the surface, the particles will have a hydrophobic and inert surface. Similarly, if the aim is to go the other way around and study the movement of the matrix-elements more in detail, fluorescent particles can be modified with surface-attached ligands that will bind to collagens.

6.3.3 Combined

Previous studies have performed individual microscopy and rheology experiments on gelation, that would afterwards be compared to reveal the link between structural and viscoelastic properties of the assembling networks. These studies have had to take into account the systematic errors from comparing two different measurements on different samples. Although the samples would be prepared as iden-

tical as possible, subtle changes in e.g. incubation time, temperature, or sample-volume resulting from the different methods, would have some effect on the network. The results from these studies can therefore not be directly compared, but have to take into consideration the probable systematic errors. Since this experiment performs microrheology-measurements and microscopy on the same samples at the same, one can say with certainty that all parameters are the same for the the measurements. This enables direct comparison of rheology and structure, an until now unachieved insight.

Whichever errors occur in the samples, being drift in the sample, airbubbles, or high-concentration regions as were the main issues in this experiment, at least the results from TL-CRM and MPT would agree in their deviations. Both results are effected equally, and so the comparison is still valid. Taking the large drift observed in the first time-points of MPT and especially in the 0.05mg/ml G-block sample as an example, this erroneous particle movement could quickly be explained by seeing the timelapse of reflectance images, and seeing a large drift in the whole samples at these timepoints. Similarly, the underlying reasons for clustering of particles in MPT could usually be difficult to explain, but with simultaneous CRM-imaging collagen-lumps could be quickly be identified as the culprits.

TL-CRM and MPT are both in principle non-invasive methods, and should not affect the self-assembly of collagen. TL-CRM visualises fibres without the need for prior staining or slicing of the specimen, and the driving forces in particle motion are to small to invoke sample deformation or disturbance of the microstructure. The fluorescent particles used for multiple particle tracking are visible in CRM images, as they reflect light at 400nm, yet their small size (500nm diameter) and relatively low number makes them only a minor disturbance when observing the collagen fibres, and they did not interfere with the fibre-analysis programs developed for this study. This new approach combining TL-CRM and MPT can be applied to other sol-gel transitions, provided the solution is transparent and the biopolymers reflect light.

6.4 Future work

This thesis is a time-limited study taking place over the course of a year. With more time other experiments could be performed to give a better picture of the effect on G-blocks on collagen network structure and viscoelastic properties. Following are some recommendations and suggestions for future work that could lead to

enhanced understanding of how G-blocks could potentially be applied in cancer treatments.

A simple way to determine if there is in fact electrostatic interactions between the anionic guluronate and positive regions on collagen is by varying the ionic strength. Upon addition of a larger amount of ionic species, there will be a screening of the charges on collagen and the G-blocks, abolishing the electrostatic interactions between them. As has been demonstrated in many of the studies on the influence on collagen gels by anionic polysaccharides.

The effect of M-blocks could be more thoroughly investigated. Although G-blocks have been investigates in this study because of their promising results form *in vivo* studies, M- and MG-blocks effects on the kinetics of collagen fibrillogenesis could provide a better understanding of the importance of structure and geometry of the oligomers in the interaction between alginates and collagen. Similarly, the polydisperse number-averaged G-block samples in this experiments could be fractioned into specific chain-lengths. Already in this experiments, there have been strong indications that some chain-lengths have a stronger effect than others, and by fractioning and purification of the samples, valuable insight on what chains are most influential on collagen fibrillation could be achieved. For future studies comparing effects of different chain-lengths the alginate concentration should be based on final molar concentrations rather than percentage by weight, to ensure the number of alginate molecules remains comparable between samples.

As discussed in the MPT-section of the Discussion, PEGylation of fluorescent spheres, or attachment of collagen-binding "linkers" can help to better distinguish between the microrheology within pores or the bulk fluid properties of the developing gel. Another approach using different sizes of (preferably PEGylated) fluorescent spheres can provide information on the pore-sizes of the gel. When particle-sizes approaches the size of the fluid pores, they exhibit a mesoscopic diffusion-pattern where they might be entrapped in one pore on a short timescale, but can "escape" and move into another pore on a larger timescale. A better understanding of the G-blocks effect on the pore-sizes of the collagen network is an important factor when attempting to modulate the biological-barrier properties of the ECM for drug-delivery.

The kinetics of the G-block-collagen interaction can be studid more in detail. This study suggested that G-blocks primarily affect the nucleation stage of fibrillogenesis. Addition of G-blocks at later timepoints in the gelation, can determine if the

effect is solely on the nucleation-stage or if the lateral-growth of nuclei into fibers are also affected. Another experiment that can be insightful and simple to perform is to investigate the temperature-dependency of the collagen-G-block interaction which can further inform on the kinetics of the interaction. It would be interesting to monitor the structure of the gel for a longer duration after the completion of the network. Although no substantial differences were observed between the overnight incubated samples and those that had been monitored for 90min, it would be of interest to observe the remodelling of the same structures in the fibre-network over time.

As discussed in the *in vivo-in vitro* section, an isolated system of only type I collagen is not comparable to the complex ECM existing *in vivo*. G-blocks might interact with any other component of the ECM, leading to the downstream effect on the collage network-structure. Further work might try to narrow down this knowledge-gap between the *in vivo-* and *in vitro* systems, by adding more components of the ECM into the system. For example working with Matrigel (extract from Engelbreth-Holm-Swarm (EHS) mouse sarcoma), replicates the ECM of tumours so that the *in vitro* self-assembly of all the components of the ECM can be monitored with G-block treatment.

7 Conclusion

The effect of alginate derived guluronate oligomers (G-blocks) on the self-assembly of type I collagen was investigated to further understand the mechanism of action of Rixova, a novel drug-candidate based on G-block technology. In this study the G-blocks have shown a marked influence on collagen network-structure and viscoelastic properties of the gel. The shortest oligomers investigated with DPn-12 (number-average degree of polymerisation) showed the most prominent effect on the collagen fibrillation. With increasing G-block concentrations the fibres increased in number and sizes, and the final network consisted of thicker fibres organised in a more intertwined and densely connected network.

Timelapse confocal reflectance microscopy (TL-CRM) was employed to investigate the kinetics of the collagen fibrillation. The G-blocks affected the rate of type 1 collagen self-assembly by accelerating the nucleation-stage of the nucleation and growth of fibres. This indicates that the G-blocks might stabilise the tropocollagen monomers, possibly by electrostatic interactions between the anionic guluronate and positive charges on the collagen-rods, facilitating the entropy-driven self-assembly of monomers into aggregates. G-blocks did not appear to affect the growth-rate of the primary aggregates into fibres, and the larger fibre-diameters observed in the final networks is likely a result of the premature aggregation in agreement with the existing model for mechanism of collagen fibrillation.

Suspended fluorescent particles were used to monitor the microrheology of the collagen sample throughout the sol-gel transition by multiple-particle tracking (MPT) and MSD-analysis of the trajectories. The addition of G-blocks resulted in an accelerated development of viscoelastic properties, corresponding to the accelerated development of fibres observed by TL-CRM. With increasing G-block concentrations the particles exhibited earlier sub-diffusive motion patterns resulting from increasing viscosity of the fluid within pores of the network, and increasing confinement by the surrounding network-structures.

The therapeutic potential of G-blocks as an anti-cancer agent has been neither affirmed nor rejected by the results from this thesis. There is a clear difference in the structure and mechanical properties of the collagen network following from the interaction with G-blocks. However, the dense network of thick fibres observed by G-block treatment in this experiment is quite opposite to the "patchy" and incomplete network formation that has been observed from G-block treatment in vivo. Further investigation is needed to better understand the collagen-modifying

potential of G-blocks in more complex *in vivo* systems.

The simultaneous monitoring of both the collagen self-assembly by TL-CRM and the mobility of the included particles by MPT and MSD-analysis, proved to be a good tool for measuring gelation of the collagen solution. Previous studies comparing rheological measurements and imaging of network-structure individually have had the issue of poor comparability of the results. By performing both measurement on the *same* samples at the *same* times, direct comparison of micro-rheology and structure of the gel could be made. This method has provided an until now unachieved insight on the correlation between these properties of the sol-gel transition, which has the potential to be applied in investigations of other biopolymers.

References

[1] Ervik M Dikshit R Eser S Mathers C Rebelo M Parkin DM Forman D Bray F. Ferlay J, Soerjomataram I. Globocan 2012 v1.0, cancer incidence and mortality worldwide: Iarc cancerbase no. 11 [internet]. 2013. URL `http://globocan.iarc.fr`.

[2] F. Mbeunkui and D. J. Johann. Cancer and the tumor microenvironment: a review of an essential relationship. *Cancer Chemother Pharmacol*, 63(4): 571–82, 2009. ISSN 0344-5704 (Print). doi: 10.1007/s00280-008-0881-9.

[3] D. F. Quail and J. A. Joyce. Microenvironmental regulation of tumor progression and metastasis. *Nature medicine*, 19(11):1423–1437, 2013. ISSN 1078-8956 1546-170X. doi: 10.1038/nm.3394. URL `http://www.ncbi.nlm.nih.gov/pmc/articles/PMC3954707/`.

[4] Fabienne Danhier, Olivier Feron, and Véronique Préat. To exploit the tumor microenvironment: Passive and active tumor targeting of nanocarriers for anti-cancer drug delivery. *Journal of Controlled Release*, 148(2): 135 – 146, 2010. ISSN 0168-3659. doi: http://dx.doi.org/10.1016/j.jconrel.2010.08.027. URL `http://www.sciencedirect.com/science/article/pii/S0168365910007108`.

[5] B. Alberts, A. Johnson, J. Lewis, D. Morgan, M. Raff, K. Roberts, and P. Walter. *Molecular Biology of the Cell, Sixth Edition:*. Taylor & Francis Group, 2014. ISBN 9781317563754. URL `https://books.google.no/books?id=jK6UBQAAQBAJ`.

[6] G. Karp. *Cell and Molecular Biology: Concepts and Experiments 6th Edition Binder Ready Version with Binder Ready Survey Flyer Set*. John Wiley & Sons, Incorporated, 2010. ISBN 9780470929667. URL `https://books.google.no/books?id=bHCXuAAACAAJ`.

[7] M. Egeblad, M. G. Rasch, and V. M. Weaver. Dynamic interplay between the collagen scaffold and tumor evolution. *Curr Opin Cell Biol*, 22(5):697–706, 2010. ISSN 0955-0674 (Print). doi: 10.1016/j.ceb.2010.08.015.

[8] Jordi Bella and David J. S. Hulmes. *Fibrillar Collagens*, pages 457–490. Springer International Publishing, Cham, 2017. ISBN 978-3-319-49674-0. doi: 10.1007/978-3-319-49674-0_14. URL `https://doi.org/10.1007/978-3-319-49674-0_14`.

[9] Thomas E. Kruger, Andrew H. Miller, and Jinxi Wang. Collagen scaffolds in bone sialoprotein-mediated bone regeneration. *The Scientific World Journal*, 2013:6, 2013. doi: 10.1155/2013/812718. URL `http://dx.doi.org/10.1155/2013/812718`.

[10] Karl E Kadler, Adele Hill, and Elizabeth G Canty-Laird. Collagen fibrillogenesis: fibronectin, integrins, and minor collagens as organizers and nucleators. *Current Opinion in Cell Biology*, 20(5):495 – 501, 2008. ISSN 0955-0674. doi: https://doi.org/10.1016/j.ceb.2008.06.008. URL `http://www.sciencedirect.com/science/article/pii/S095506740800118X`. Cell-to-cell contact and extracellular matrix.

[11] M. Djabourov, J. P. Lechaire, and F. Gaill. Structure and rheology of gelatin and collagen gels. *Biorheology*, 30(3-4):191–205, 1993. ISSN 0006-355X (Print) 0006-355x.

[12] Barbara Brodsky and John A.M. Ramshaw. The collagen triple-helix structure. *Matrix Biology*, 15(8):545 – 554, 1997. ISSN 0945-053X. doi: https://doi.org/10.1016/S0945-053X(97)90030-5. URL `http://www.sciencedirect.com/science/article/pii/S0945053X97900305`.

[13] Y. Li. *The Mechanism of Collagen Self-assembly: Hydrophobic and Electrostatic Interactions*. University of Florida, 2009. URL `https://books.google.no/books?id=tNkmnQAACAAJ`.

[14] Adam J. Engler, Shamik Sen, H. Lee Sweeney, and Dennis E. Discher. Matrix elasticity directs stem cell lineage specification. *Cell*, 126(4):677 – 689, 2006. ISSN 0092-8674. doi: https://doi.org/10.1016/j.cell.2006.06.044. URL `http://www.sciencedirect.com/science/article/pii/S0092867406009615`.

[15] Pengfei Lu, Valerie M. Weaver, and Zena Werb. The extracellular matrix: A dynamic niche in cancer progression. *The Journal of Cell Biology*, 196(4):395–406, 2012. ISSN 0021-9525. doi: 10.1083/jcb.201102147. URL `http://jcb.rupress.org/content/196/4/395`.

[16] M. Egeblad, M. G. Rasch, and V. M. Weaver. Dynamic interplay between the collagen scaffold and tumor evolution. *Curr Opin Cell Biol*, 22(5):697–706, 2010. ISSN 0955-0674 (Print). doi: 10.1016/j.ceb.2010.08.015.

[17] M. Fang, J. Yuan, C. Peng, and Y. Li. Collagen as a double-edged sword in tumor progression. *Tumour Biol*, 35(4):2871–82, 2014. ISSN 1010-4283 (Print). doi: 10.1007/s13277-013-1511-7.

[18] Matthew J. Paszek, Nastaran Zahir, Kandice R. Johnson, Johnathon N. Lakins, Gabriela I. Rozenberg, Amit Gefen, Cynthia A. Reinhart-King, Susan S. Margulies, Micah Dembo, David Boettiger, Daniel A. Hammer, and Valerie M. Weaver. Tensional homeostasis and the malignant phenotype. *Cancer Cell*, 8(3):241 – 254, 2005. ISSN 1535-6108. doi: https://doi.org/10.1016/j.ccr.2005.08.010. URL `http://www.sciencedirect.com/science/article/pii/S1535610805002680`.

[19] Chrisostomi Gialeli, Achilleas D. Theocharis, and Nikos K. Karamanos. Roles of matrix metalloproteinases in cancer progression and their pharmacological targeting. *The FEBS Journal*, 278(1):16–27. doi: 10.1111/j.1742-4658.2010.07919.x. URL `https://febs.onlinelibrary.wiley.com/doi/abs/10.1111/j.1742-4658.2010.07919.x`.

[20] T. Liu, O. A. Babaniyi, T. J. Hall, P. E. Barbone, and A. A. Oberai. Non-invasive in-vivo quantification of mechanical heterogeneity of invasive breast carcinomas. *PLoS One*, 10(7), 2015. doi: 10.1371/journal.pone.0130258.

[21] Paolo P. Provenzano, Kevin W. Eliceiri, Jay M. Campbell, David Inman, John George White, and Patricia J. Keely. Collagen reorganization at the tumor-stromal interface facilitates local invasion. *BMC Medicine*, 4:38 – 38, 2006.

[22] P. P. Provenzano, D. R. Inman, K. W. Eliceiri, and P. J. Keely. Matrix density-induced mechanoregulation of breast cell phenotype, signaling and gene expression through a fak–erk linkage. *Oncogene*, 28: 4326, 2009. doi: 10.1038/onc.2009.299https://www.nature.com/articles/onc2009299#supplementary-information. URL `http://dx.doi.org/10.1038/onc.2009.299`.

[23] P. A. Netti, D. A. Berk, M. A. Swartz, A. J. Grodzinsky, and R. K. Jain. Role of extracellular matrix assembly in interstitial transport in solid tumors. *Cancer Res*, 60(9):2497–503, 2000. ISSN 0008-5472 (Print) 0008-5472.

[24] Markus Loeffler, Jörg A. Krüger, Andreas G. Niethammer, and Ralph A. Reisfeld. Targeting tumor-associated fibroblasts improves cancer chemotherapy by increasing intratumoral drug uptake. *The Journal of Clinical Investigation*, 116(7):1955–1962, 7 2006. doi: 10.1172/JCI26532. URL `https://www.jci.org/articles/view/26532`.

[25] K. P. Olive, M. A. Jacobetz, C. J. Davidson, A. Gopinathan, D. McIntyre, D. Honess, B. Madhu, M. A. Goldgraben, M. E. Caldwell, D. Allard, K. K. Frese, G. Denicola, C. Feig, C. Combs, S. P. Winter, H. Ireland-Zecchini, S. Reichelt, W. J. Howat, A. Chang, M. Dhara, L. Wang, F. Ruckert, R. Grutzmann, C. Pilarsky, K. Izeradjene, S. R. Hingorani, P. Huang, S. E. Davies, W. Plunkett, M. Egorin, R. H. Hruban, N. Whitebread, K. McGovern, J. Adams, C. Iacobuzio-Donahue, J. Griffiths, and D. A. Tuveson. Inhibition of hedgehog signaling enhances delivery of chemotherapy in a mouse model of pancreatic cancer. *Science*, 324(5933):1457–61, 2009. ISSN 0036-8075. doi: 10.1126/science.1171362.

[26] Kurt Draget, Olav Smidsrød, and Gudmund Skjåk-Bræk. Alginates from algae. 6, 01 2005.

[27] David L. Nelson, David L. Nelson, Albert L. Lehninger, and Michael M. Cox. *Lehninger principles of biochemistry*. W.H. Freeman, New York, 2008. ISBN 071677108X 9780716771081 9781429208925 1429208929.

[28] Genaro Paredes-Juarez, Milica Spasojevic, Marijke Faas, and Paul de Vos. Immunological and technical considerations in application of alginate-based microencapsulation systems. 2:1–15, 08 2014.

[29] Kuen Yong Lee and David J. Mooney. Alginate: properties and biomedical applications. *Progress in polymer science*, 37 1:106–126, 2012.

[30] K. I. Draget and O. Smidsrød. Modification of gelling kinetics and elastic properties by nano structuring of alginate gels exploiting the properties of poly-guluronate. *In Proceedings from the 13th Gums and Stabilisers Conference for the Food Industry*, page 227, 2006.

[31] Gregor T. Grant, Edwin R. Morris, David A. Rees, Peter J.C. Smith, and David Thom. Biological interactions between polysaccharides and divalent cations: The egg-box model. *FEBS Letters*, 32(1):195 – 198, 1973. ISSN 0014-5793. doi: https://doi.org/10.1016/0014-5793(73)80770-7. URL http://www.sciencedirect.com/science/article/pii/0014579373807707.

[32] Jerome P. Paques, Erik van der Linden, Cees J.M. van Rijn, and Leonard M.C. Sagis. Preparation methods of alginate nanoparticles. *Advances in Colloid and Interface Science*, 209:163 – 171, 2014. ISSN 0001-8686. doi: https://doi.org/10.1016/j.cis.2014.03.009. URL http://www.sciencedirect.com/science/article/pii/S0001868614001341.

[33] M. Otterlei, K. Ostgaard, G. Skjak-Braek, O. Smidsrod, P. Soon-Shiong, and T. Espevik. Induction of cytokine production from human monocytes stimulated with alginate. *J Immunother (1991)*, 10(4):286–91, 1991. ISSN 1053-8550 (Print) 1053-8550.

[34] Catherine Taylor Nordgård, Unni Nonstad, Magnus Ø. Olderøy, Terje Espevik, and Kurt I. Draget. Alterations in mucus barrier function and matrix structure induced by guluronate oligomers. *Biomacromolecules*, 15(6):2294–2300, 2014. doi: 10.1021/bm500464b. URL `https://doi.org/10.1021/bm500464b`. PMID: 24827030.

[35] Megan Vitko, Dana M. Valerio, Philip D. Rye, Edvar Onsøyen, Astrid H. Myrset, Arne Dessen, Mitchell L. Drumm, and Craig A. Hodges. A novel guluronate oligomer improves intestinal transit and survival in cystic fibrosis mice. *Journal of Cystic Fibrosis*, 15(6):745 – 751, 2016. ISSN 1569-1993. doi: https://doi.org/10.1016/j.jcf.2016.06.005. URL `http://www.sciencedirect.com/science/article/pii/S1569199316305483`.

[36] Catherine Taylor Nordgård and Kurt Draget. Uses of oligouronates in cancer treatment (2014), wo2014ep79178 20141223.

[37] Andrew O. Brightman, Bartłomiej Rajwa, Jennifer E Sturgis, Morgan McCallister, J. Paul Robinson, and Sherry L Voytik-Harbin. Time-lapse confocal reflection microscopy of collagen fibrillogenesis and extracellular matrix assembly in vitro. *Biopolymers*, 54 3:222–34, 2000.

[38] M. de Wild, W. Pomp, and H. Koenderink G . Thermal memory in self-assembled collagen fibril networks. *Biophys J*, 105(1):200–10, 2013. ISSN 0006-3495 (Print). doi: 10.1016/j.bpj.2013.05.035.

[39] Marcus E. Carr and Jan Hermans. Size and density of fibrin fibers from turbidity. *Macromolecules*, 11(1):46–50, 1978. doi: 10.1021/ma60061a009. URL `http://dx.doi.org/10.1021/ma60061a009`.

[40] Jieling Zhu and Laura J Kaufman. Collagen i self-assembly: Revealing the developing structures that generate turbidity. *Biophysical Journal*, 106(8):1822–1831, 2014. ISSN 0006-3495 1542-0086. doi: 10.1016/j.bpj.2014.03.011. URL `http://www.ncbi.nlm.nih.gov/pmc/articles/PMC4008796/`.

[41] L. Taiz and E. Zeiger. *Plant Physiology and Development*. Sinauer, 2014. ISBN 9781605352558. URL `https://books.google.no/books?id=frXboQEACAAJ`.

[42] Marjan Shayegan and Nancy Forde. Microrheological characterization of collagen systems: From molecular solutions to fibrillar gels. 8:e70590, 08 2013.

[43] M. Minsky. Memoir on inventing the confocal scanning microscope. *Scanning*, 10(4):128–138. doi: 10.1002/sca.4950100403. URL `https://onlinelibrary.wiley.com/doi/abs/10.1002/sca.4950100403`.

[44] Moeen Ghafoor. Synthesis of high refractive index materials for manufacturing apochromatic lens by 3d printing. 10 2017.

[45] Junghae Suh, Michelle Dawson, and Justin Hanes. Real-time multiple-particle tracking: applications to drug and gene delivery. *Advanced Drug Delivery Reviews*, 57(1):63 – 78, 2005. ISSN 0169-409X. doi: https://doi.org/10.1016/j.addr.2004.06.001. URL `http://www.sciencedirect.com/science/article/pii/S0169409X04001851`. Advances in Fluorescence Imaging: Opportunities for Pharmaceutical Science.

[46] Nicolas Chenouard, Ihor Smal, Fabrice de Chaumont, Martin Maška, Ivo F. Sbalzarini, Yuanhao Gong, Janick Cardinale, Craig Carthel, Stefano Coraluppi, Mark Winter, Andrew R. Cohen, William J. Godinez, Karl Rohr, Yannis Kalaidzidis, Liang Liang, James Duncan, Hongying Shen, Yingke Xu, Klas E. G. Magnusson, Joakim Jaldén, Helen M. Blau, Perrine Paul-Gilloteaux, Philippe Roudot, Charles Kervrann, François Waharte, Jean-Yves Tinevez, Spencer L. Shorte, Joost Willemse, Katherine Celler, Gilles P. van Wezel, Han-Wei Dan, Yuh-Show Tsai, Carlos Ortiz de Solórzano, Jean-Christophe Olivo-Marin, and Erik Meijering. Objective comparison of particle tracking methods. *Nature Methods*, 11:281, 2014. doi: 10.1038/nmeth.2808https://www.nature.com/articles/nmeth.2808#supplementary-information. URL `http://dx.doi.org/10.1038/nmeth.2808`.

[47] John C. Crocker and David G. Grier. Methods of digital video microscopy for colloidal studies. *Journal of Colloid and Interface Science*, 179 (1):298 – 310, 1996. ISSN 0021-9797. doi: https://doi.org/10.1006/jcis.1996.0217. URL `http://www.sciencedirect.com/science/article/pii/S0021979796902179`.

[48] Thierry Savin and Patrick S. Doyle. Static and dynamic errors in particle tracking microrheology. *Biophysical Journal*, 88(1):623 – 638, 2005. ISSN 0006-3495. doi: https://doi.org/10.1529/biophysj.104.042457. URL `http://www.sciencedirect.com/science/article/pii/S0006349505731362`.

[49] Thomas Moschakis. Microrheology and particle tracking in food gels and emulsions. *Current Opinion in Colloid l& Interface Science*, 18(4): 311 – 323, 2013. ISSN 1359-0294. doi: https://doi.org/10.1016/j.cocis. 2013.04.011. URL `http://www.sciencedirect.com/science/article/pii/S135902941300068X`.

[50] Curtis T. Rueden, Johannes Schindelin, Mark C. Hiner, Barry E. DeZonia, Alison E. Walter, Ellen T. Arena, and Kevin W. Eliceiri. Imagej2: Imagej for the next generation of scientific image data. *BMC Bioinformatics*, 18 (1):529, Nov 2017. ISSN 1471-2105. doi: 10.1186/s12859-017-1934-z. URL `https://doi.org/10.1186/s12859-017-1934-z`.

[51] MATLAB. *version 8.3.0.532 (R2014a)*. The MathWorks Inc., Natick, Massachusetts, 2014.

[52] Stormy Attaway. *Matlab, Third Edition: A Practical Introduction to Programming and Problem Solving*. Butterworth-Heinemann, Newton, MA, USA, 3rd edition, 2013. ISBN 0124058760, 9780124058767.

[53] I.F. Sbalzarini and P. Koumoutsakos. Feature point tracking and trajectory analysis for video imaging in cell biology. *Journal of Structural Biology*, 151(2):182 – 195, 2005. ISSN 1047-8477. doi: https://doi.org/10.1016/j. jsb.2005.06.002. URL `http://www.sciencedirect.com/science/article/pii/S1047847705001267`.

[54] Johannes Schindelin, Ignacio Arganda-Carreras, Erwin Frise, Verena Kaynig, Mark Longair, Tobias Pietzsch, Stephan Preibisch, Curtis Rueden, Stephan Saalfeld, Benjamin Schmid, Jean-Yves Tinevez, Daniel James White, Volker Hartenstein, Kevin Eliceiri, Pavel Tomancak, and Albert Cardona. Fiji: an open-source platform for biological-image analysis. *Nature Methods*, 9(7):676 – 682, 2012. ISSN 15487091. URL `http://search.ebscohost.com/login.aspx?direct=true&db=a9h&AN=77406531&site=ehost-live`.

[55] Nadine Tarantino, Jean-Yves Tinevez, Elizabeth Faris Crowell, Bertrand Boisson, Ricardo Henriques, Musa Mhlanga, Fabrice Agou, Alain Israël, and Emmanuel Laplantine. Tnf and il-1 exhibit distinct ubiquitin requirements for inducing nemo–ikk supramolecular structures. *The Journal of Cell Biology*, 204(2):231–245, 2014. ISSN 0021-9525. doi: 10.1083/jcb.201307172. URL `http://jcb.rupress.org/content/204/2/231`.

[56] Gloria A Di Lullo, Shawn M Sweeney, Jarmo Korkko, Leena M Ala-Kokko, and James D. San Antonio. Mapping the ligand-binding sites and disease-associated mutations on the most abundant protein in the human, type i collagen. *The Journal of biological chemistry*, 277 6:4223–31, 2002.

[57] Jeremy Mark Berg, John L. Tymoczko, and Lubert Stryer. *Biochemistry.* W.H. Freeman, Basingstoke, 2012. ISBN 9781429276351 1429276355.

[58] Kate Stuart and Alyssa Panitch. Influence of chondroitin sulfate on collagen gel structure and mechanical properties at physiologically relevant levels. *Biopolymers*, 89(10):841–851. doi: 10.1002/bip.21024. URL `https://onlinelibrary.wiley.com/doi/abs/10.1002/bip.21024`.

[59] Shiao-Wen Tsai, Re-Lin Liu, Fu-Yin Hsu, and Chia-Chun Chen. A study of the influence of polysaccharides on collagen self-assembly: Nanostructure and kinetics. 83:381–8, 11 2006.

[60] B. Obrink. A study of the interactions between monomeric tropocollagen and glycosaminoglycans. *Eur J Biochem*, 33(2):387–400, 1973. ISSN 0014-2956 (Print) 0014-2956.

[61] Xuejun Xin, Assunta Borzacchiello, Paolo Netti, Luigi Ambrosio, and Luigi Nicolais. Hyaluronic-acid-based semi-interpenetrating materials. 15:1223–36, 02 2004.

[62] G. C. Wood. The formation of fibrils from collagen solutions. 3. effect of chondroitin sulphate and some other naturally occurring polyanions on the rate of formation. *Biochem J*, 75(3):605–12, 1960. ISSN 0264-6021 (Print).

[63] Katrin Salchert, Uwe Streller, Tilo Pompe, Nicole Herold, Milauscha Grimmer, and Carsten Werner. In vitro reconstitution of fibrillar collagen type i assemblies at reactive polymer surfaces. *Biomacromolecules*, 5(4):1340–1350, 2004. doi: 10.1021/bm0499031. URL `https://doi.org/10.1021/bm0499031`. PMID: 15244449.

[64] Dimitar Stamov, Milauscha Grimmer, Katrin Salchert, Tilo Pompe, and Carsten Werner. Heparin intercalation into reconstituted collagen i fibrils: Impact on growth kinetics and morphology. *Biomaterials*, 29(1):1 – 14, 2008. ISSN 0142-9612. doi: https://doi.org/10.1016/j.biomaterials.2007.09.009. URL `http://www.sciencedirect.com/science/article/pii/S0142961207007132`.

[65] Susanne Bierbaum, Timothy Douglas, Thomas Hanke, Dieter Scharnweber, Sonja Tippelt, Thomas K. Monsees, Richard H. W. Funk, and Hartmut Worch. Collageneous matrix coatings on titanium implants modified with decorin and chondroitin sulfate: Characterization and influence on osteoblastic cells. *Journal of Biomedical Materials Research Part A*, 77A(3):551–562. doi: 10.1002/jbm.a.30572. URL `https://onlinelibrary.wiley.com/doi/abs/10.1002/jbm.a.30572`.

[66] Y. Nomura, Y. Ishii, and K. Takahashi. Control of collagen molecular assembly with anionic polysaccharides. *Biosci Biotechnol Biochem*, 73(4):926–9, 2009. ISSN 0916-8451.

[67] Lin Sang, Xiaoliang Wang, Zhenhua Chen, Jiao Lu, Zhongwei Gu, and Xudong Li. Assembly of collagen fibrillar networks in the presence of alginate. *Carbohydrate Polymers*, 82(4):1264 – 1270, 2010. ISSN 0144-8617. doi: https://doi.org/10.1016/j.carbpol.2010.07.005. URL `http://www.sciencedirect.com/science/article/pii/S0144861710005394`.

[68] Matthew D. Shoulders and Ronald T. Raines. Collagen structure and stability. *Annual review of biochemistry*, 78:929–958, 2009. ISSN 0066-4154 1545-4509. doi: 10.1146/annurev.biochem.77.032207.120833. URL `http://www.ncbi.nlm.nih.gov/pmc/articles/PMC2846778/`.

[69] Huilin Tian, Yihui Chen, Cuicui Ding, and Guoying Li. Interaction study in homogeneous collagen/chondroitin sulfate blends by two-dimensional infrared spectroscopy. *Carbohydrate Polymers*, 89(2):542 – 550, 2012. ISSN 0144-8617. doi: https://doi.org/10.1016/j.carbpol.2012.03.042. URL `http://www.sciencedirect.com/science/article/pii/S014486171200269X`.

[70] J D San Antonio, A D Lander, M J Karnovsky, and H S Slayter. Mapping the heparin-binding sites on type i collagen monomers and fibrils. *The Journal of Cell Biology*, 125(5):1179–1188, 1994. ISSN 0021-9525. doi: 10.1083/jcb.125.5.1179. URL `http://jcb.rupress.org/content/125/5/1179`.

A HPAEC-PAD (Dionex)

A.1 G-blocks M-blocks

G-blokk

M og MG-blokk
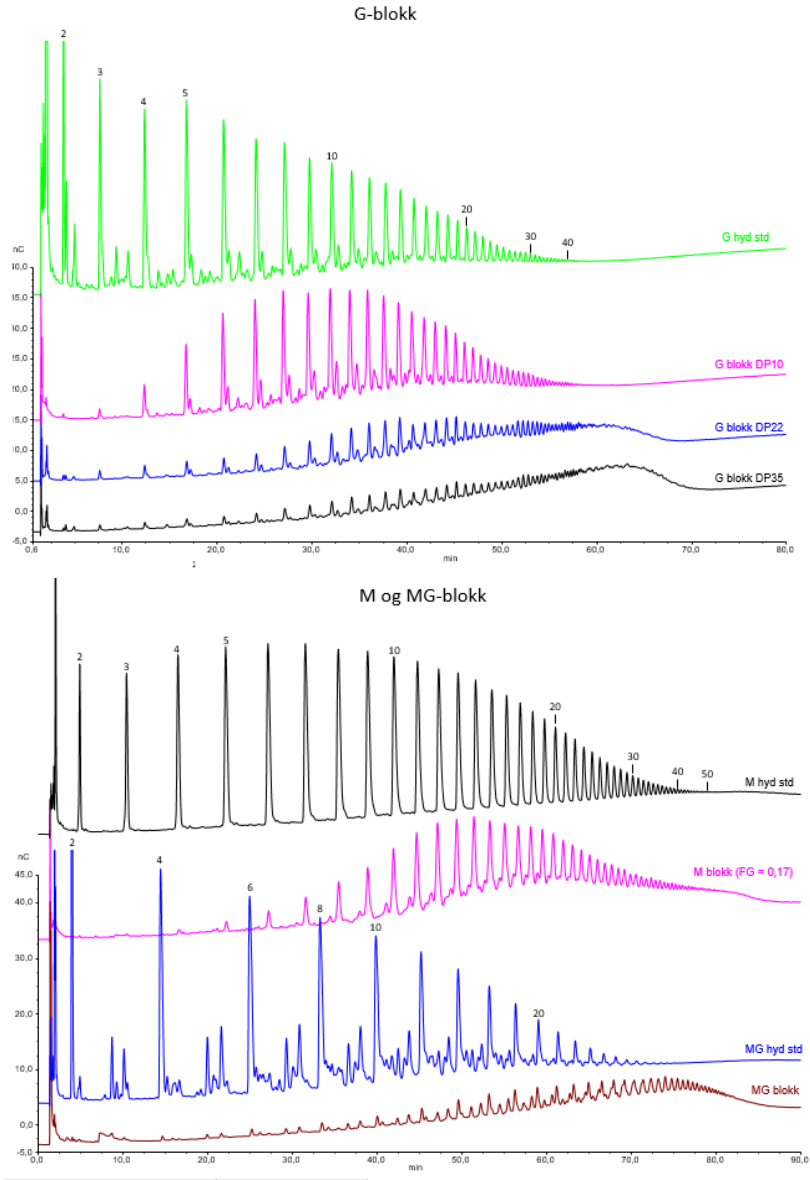
A.2 G-block DPn-12
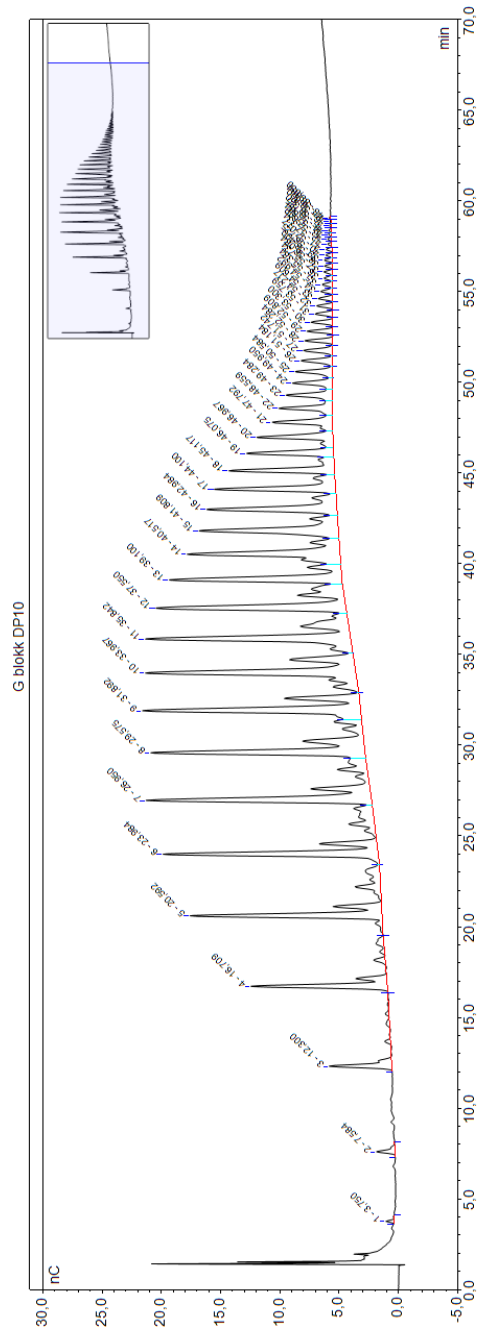
B Microscope-settings

B.1 Reflection-mode(TL-CRM)

Dimension	Logical Size	Physical Length	Start Position	End Position	Pixel Size / Voxel Size
X	2232	232.5 µm	0 µm	232.5 µm	0.104 µm
Y	2232	232.5 µm	0 µm	232.5 µm	0.104 µm
Z	1	0 µm	0 µm	0 µm	0 µm
Loop	36	0	0	0	

Channels

LUT		Resolution	Min	Max	STED: DetectorMode / Huygens saturation factor / Wavelength
Green		8	0	255	--- / --- / ---

Time Stamps:

Frame (Show All)	Relative Time (s)	Absolute Time (h:m:s.ms)	Date
1	0,000	12.16.34.294	30.03.2018
36	5304,777	13.44.59.071	30.03.2018

Confocal Settings

Name	Value
Rotator Angle	0 °
Scan Mode	xyz
Scan Direction X	Unidirectional
Scan Speed	100 Hz
Version Number	10
StagePosX	58,000.15 µm
StagePosY	46,000.06 µm
ZPosition	0 µm
IsSuperZ	0
Magnification	25
ObjectiveName	HCX IRAPO L 25x/0.95 WATER
Immersion	WATER
NumericalAperture	0.95
RefractionIndex	1.33
Zoom	2

III

Pinhole	55.9 µm
PinholeAiry	1 AU
EmissionWavelength for PinholeAiry Calculation	580 nm
FrameAverage	1
LineAverage	3
FrameAccumulation	1
Line_Accumulation	1
IsUserSettingNameSet	0
IsRoiScanEnable	0

Filter Wheels / Other Motorized Devices

Device Name	Filter Name/Position
Attenuation MP	Min
External Detection FW	Mirror
FCS-FW	---
Galvo Slider	Galvo X Normal
Multi Function Port	Substrate
Notch FW 2	Empty
Polarization FW	Empty
Galvo Resonant Pan	Galvo X Pan Center
Target Slider	Target Park
X2 Lens Changer	CS2 UV Optics 1

Lasers

LaserName	OutputPower
WLL	**On, 70,0000 %**
IR	**On**

Laser Lines

Laser Line	Intensity
Supercontinuum Visible (488 nm)	Shutter: on, Intensity: 4.6223%

Detectors

Name	Channel	Type	Location	Active	Gain	Offset	Gate Start	Gate End	Gate Ref. Wavelength
HyD 1	Channel 1	HyD (485nm - 497nm) Standard mode	Internal	Active	121	-0.01		-- Time Gating not activated --	

B.2 Flourescence-mode (MPT)

Dimensions

Dimension	Logical Size	Physical Length	Start Position	End Position	Pixel Size / Voxel Size
X	512	232.5 µm	0 µm	232.5 µm	0.455 µm
Y	512	232.5 µm	0 µm	232.5 µm	0.455 µm
T	28	19,980 s	0 s	19,980 s	0,740 s
Loop	37	0	0	0	

Channels

LUT		Resolution	Min	Max	STED: DetectorMode / Huygens saturation factor / Wavelength
Green		8	0	255	--- / --- / ---

Time Stamps:

Frame (Show All)	Relative Time (s)	Absolute Time (h:m:s.ms)	Date
1	0,000	12.16.38.213	30.03.2018
1009	5324,736	13.45.22.949	30.03.2018

Confocal Settings

Name	Value
Rotator Angle	0 °
Scan Mode	xyt
Scan Direction X	Unidirectional
Scan Speed	700 Hz
Version Number	10
StagePosX	58,000 µm
StagePosY	46,000.17 µm
ZPosition	0 µm
IsSuperZ	0
Magnification	25
ObjectiveName	HCX IRAPO L 25x/0.95 WATER
Immersion	WATER
NumericalAperture	0.95
RefractionIndex	1.33
Zoom	2
Pinhole	55.9 µm
PinholeAiry	1 AU
EmissionWavelength for PinholeAiry Calculation	580 nm
FrameAverage	1

LineAverage	1
FrameAccumulation	1
Line_Accumulation	1
IsUserSettingNameSet	0

Filter Wheels / Other Motorized Devices

Device Name	Filter Name/Position
Attenuation MP	Min
External Detection FW	Mirror
FCS-FW	---
Galvo Slider	Galvo X Normal
Multi Function Port	Substrate
Notch FW 2	Empty
Polarization FW	NF 488
Galvo Resonant Pan	Galvo X Pan Center
Target Slider	Target Park
X2 Lens Changer	CS2 UV Optics 1

Lasers

LaserName	OutputPower
WLL	On, 70,0000 %
IR	On

Laser Lines

Laser Line	Intensity
Supercontinuum Visible (488 nm)	Shutter: on, Intensity: 6.3741%

Detectors

Name	Channel	Type	Location	Active	Gain	Offset	Gate Start	Gate End	Gate Ref. Wavelength
PMT 2	Channel 2	PMT (495nm - 561nm)	Internal	Active	772.2	0	-- Time Gating not supported --		

C MATLAB functions for fiberanalysis

C.1 num_peaks

```matlab
function [ peaks , lenghts] = num_peaks ( dist ,
    intensities , cutoff)
%takes in distances(dist) and pixel-intensities(
    intensities) along an ROI-line , counting numbers of "
    peaks" and measuring their size(lengths)

log = intensities > cutoff;

peaks = 0;
onpeak = 0;

lt = NaN(1,length(log));

for i = 1:length(log)
    y = log(i);
    if y && ~onpeak
        peaks = peaks + 1;
        onpeak = 1;
        start = dist(i);
    elseif ~y && onpeak
        onpeak = 0;
        lt(peaks) = dist(i) - start;
    end
end

lenghts = nanmean(lt);
end
```

C.2 average_peaks

```
1  function [ avInt , avnrpeak , avlength ] = average_peaks (
       matrix , cutoff )
2  % Execute num_peaks for each of the 10 ROI - lines in an
       image .
3  % avInt = average pixel - intensity
4  % avnrpeak = average number of peaks encounteres along a
       ROI - line
5  % avlength = average length of a peak
6
7  dist = matrix (: , 1);
8  avInt = mean ( mean ( matrix (: , 2: size ( matrix , 2))));
9
10 for i = 2: size ( matrix , 2)
11     intensity = matrix (: , i);
12
13     [ peaks (i) , lengths (i)] = num_peaks ( dist , intensity ,
           cutoff );
14
15 end
16
17 avnrpeak = mean ( peaks );
18 avlength = mean ( lengths );
19
20 end
```

C.3 list_averages

```matlab
function [intensities, peaks, lengths] = lists_averages
    (cell)
%Enables fiberanalysis of multiple matrices within a
    cell.
%Makes list of pixel-intensity, number of peaks and
    length of peaks from each timepoint

cutoff = mean(mean(cell{1}(:, 2:size(cell{1}, 2)))) + 10
    ;
%cutoff generated from first matrix of the cell (first
    time-point)

for i = 1:length(cell)
    matrix = cell{i};

    [intensities(i), peaks(i), lengths(i)] =
        average_peaks(matrix, cutoff);

end
end
```

D   MATLAB - MSD-analysis

D.1   MakeCell

```matlab
function tracks = makeCell(matrix)
%composes a matrix of particle trajectories into a cell
trajectories = length(unique(matrix(:,2)));
tracks = cell(trajectories, 1);
y = matrix(:,2);
for j = 1:trajectories
for i = 1:length(y)
    if  y(i) == j
        tracks{j,1}(i,1) = matrix(i,3)*0.74;
        tracks{j,1}(i,2) = matrix(i,4);
        tracks{j,1}(i,3) = matrix(i,5);
    end
end
tracks{j,1}( ~any(tracks{j,1},2), : ) = [];
end
end
```

D.2 MSDanalysis

```matlab
1  function [ma, mmsd, alpha] = MSDanalysis(matrix)
2  tracks = makeCell(matrix);
3  ma = msdanalyzer(2, ' m ', 's');
4  ma = ma.addAll(tracks);
5  ma = ma.computeMSD;
6
7  %plots MSD as a function of time-lag (time average)
8  figure
9  ma.plotMSD;
10
11 %computes and plots the weighted mean of all MSD curves
       (ensamble average)
12 figure
13 ma.plotMeanMSD(gca, true)
14 mmsd = ma.getMeanMSD;
15 t = mmsd(:,1);
16 x = mmsd(:,2);
17 dx = mmsd(:,3) ./ sqrt(mmsd(:,4));
18 errorbar(t, x, dx, 'k')
19
20 % curve-fitting Estimating Diffucion coefficient through
        linear weighted
21 % fit of the mean MSD curve. only made on the first 25%
       of the curve,
22 [fo, gof] = ma.fitMeanMSD;
23 plot(fo);
24 legend off
25 ma.labelPlotMSD;
26
27 %plots all MSD as a function of lagtime on a logrithmic
       scale
28 figure
29 ma.plotMSD;
30 set(gca, 'XScale', 'log')
31 set(gca, 'YScale', 'log')
```

```matlab
32  axis([0.5 30 0 1000]);
33
34  %clip-factor of 0.5, takes only into account the first
        50% portion of the MSD curve
35  ma = ma.fitLogLogMSD(0.5);
36  ma.loglogfit;
37  alpha = nanmean(ma.loglogfit.alpha);
38  end
```

D.3 Anomalous exponent distribution

```matlab
function [average, deviation] = a_distribution(ma)
ma = ma.fitLogLogMSD(0.5);
ma.loglogfit;
r2fits = ma.loglogfit.r2fit;
alphas = ma.loglogfit.alpha;

R2LIMIT = 0.8;
% Remove bad fits
bad_fits = (r2fits < R2LIMIT)  | (alphas<(0))| (alphas
    >3) | (isnan(alphas));
fprintf('Keeping %d fits (R2 > %.2f).\n', sum(~bad_fits)
    , R2LIMIT);
alphas(bad_fits) = [];

% T-test
[htest, pval] = ttest(alphas, 1, 0.05, 'left');
if ~htest
    [htest, pval] = ttest(alphas, 1, 0.05);
end

% Prepare string
str = { [ '\alpha = ' sprintf('%.2f    %.2f (mean    std
    , N = %d)', mean(alphas), std(alphas), numel(alphas))
    ] };

if htest
    str{2} = sprintf('Significantly below 1, with p =
        %.2g', pval);
else
    str{2} = sprintf('Not significantly different from
        1, with p = %.2g', pval);
end

figure
hist(alphas);
```

```matlab
30  box off
31  xlabel('\alpha')
32  ylabel('#')
33  yl = ylim(gca);
34  xl = xlim(gca);
35  text(xl(2), yl(2)+2, str, ...
36      'HorizontalAlignment', 'right', ...
37      'VerticalAlignment', 'top', ...
38      'FontSize', 16)
39  ylim([0 yl(2)+2])
40  average = mean(alphas);
41  deviation = std(alphas);
```